# MECHANICAL TESTING AND NUMERICAL SIMULATION OF MECHANICAL STRUCTURE-PROPERTY RELATIONSHIP OF SILICA AEROGEL

By

NILESH NATHU SHIMPI

Bachelor of Engineering
University of Mumbai
Mumbai, India
2001

Submitted to the Faculty of the
Graduate College of the
Oklahoma State University
in partial fulfillment of
the requirements for
the Degree of
MASTER OF SCIENCE
December , 2005

MECHANICAL TESTING AND NUMERICAL
SIMULATION OF MECHANICAL
STRUCTURE-PROPERTY RELATIONSHIP
OF SILICA AEROGEL

Thesis Approved:

Dr. Samit Roy

Thesis Adviser

Dr. Hongbing Lu

Dr. Christopher Price

Dr. A. Gordon Emslie

Dean of the Graduate College

# ACKNOWLEDGEMENTS

I wish to express my gratitude to my parents for their confidence in me. I would like to thank them for their consistent encouragement and love. I would like to express my gratitude to my sisters for their inspiration and support. My special thanks are due to my roommates for their motivation and support during my studies.

I would like to express my sincere thanks to my adviser, Dr. Samit Roy for his supervision, constructive guidance, financial support and inspiration throughout the study. I would like to thank him for providing me with sophisticated and friendly work environment. My master's study under him was a wonderful experience. I would also like to extend my sincere appreciation to Dr. Hongbing Lu and Dr. Christopher Price for providing invaluable guidance and encouragement throughout this study.

This project has been funded by the grant (NNC04GB54G) from the National Aeronautics and Space Administration (NASA), Glenn, OH. I would like to thank Dr. Nicholas Leventis and his group for their interest and support of this work. I would also like to thank Dr. Tom Haard for his discussion on diffusion limited cluster aggregation algorithm.

I wish to express my sincere gratitude to Mr. Atul Katti for his co-operation, discussions and friendship in this study. I wish to extend my gratitude to Mr. Jerry Dale for his guidance in machining and making fixtures. I would like to thank my research colleagues for their constant help and encouragement.

Finally, I would like to thank the Department of Mechanical and Aerospace Engineering for providing me with the opportunity to pursue M.S. at Oklahoma State University.

# TABLE OF CONTENTS

**Chapter** **Page**

# LIST OF TABLES

**Table** **Page**

## LIST OF FIGURES

# CHAPTER 1

# INTRODUCTION

Materials and their development are fundamental to society. Major historical periods of society are ascribed to materials (i.e., stone age, bronze age, iron age, steel age, silicon age and silica age). Scientists will open the next societal frontiers not by understanding a particular material, but rather by understanding and optimizing the relative contributions afforded by material combinations.

The nanoscale and associated nanoscience and technology afford opportunities to create revolutionary material combinations. These new materials circumvent classic material performance trade-offs by accessing new properties and exploiting synergism between materials.

Major enhancements in mechanical, rheological, dielectric, optical, and other properties of polymer materials have been achieved by additives such as carbon black, talc, silica, and other inexpensive, inorganic materials. Nanofillers such as nanotubes, silica beads and cages, and clays, offer phenomenal advantages over these more traditional fillers because greater property improvement is achieved with far less material. For example, adding 1% by weight of ultra-fine, synthetic mica (30-nm diameter disks) to

nylon gives super-tough nylon, while adding the same amount of traditional mica (micron-sized talc) gives only a slight improvement in toughness over the unfilled polymer. [1]

Major advances in the design and fabrication of new materials that are lightweight and high strength will come from advances in the fundamental understanding of nanocomposites, in which nanoscopic fillers are dispersed on nanometer scales within the polymer matrix. The growing ability to design customized nanofillers of arbitrary shape and functionality provides an enormous variety of possible property modifications by introducing specific heterogeneity at the nanoscale. However, little is known about the specific influence of nanofillers on the polymers surrounding them, and thus the development of highly designed, nanostructured materials for specific applications is currently limited. Future breakthroughs in the development of organic/inorganic hybrid nanocomposites will be possible by manipulating the inorganic phase on nanometer scales in order to achieve specific properties. Achieving such capability will require insight on many length scales, ranging from the interfacial interactions on molecular scales, to the ordering and assembly of inorganic phases on lengths scales from several tens of nanometers to tens of microns, to the manifestation of bulk material properties on macroscopic scales. Computer simulation is securely an important tool in materials discovery and optimization, and in interpreting and guiding experiments to probe and manipulate these materials on molecular scales

One of the most successful commercial uses of nanoparticles is as fillers in plastics [2]. Properties such as strength can be improved by including a small weight percent (typically less than 5%) of the filler, and significant current research is focused on

improving the chemical compatibility between the filler and the polymeric matrix. In this environment, if the amount of the filler and the polymer become compatible, then the roles of the filler and the matrix can be reversed, and if the filler, or one of its forms, has useful properties of its own, then those properties can be improved by 'doping' with a polymer [3].

The most common filler is silica, and a form of silica, the silica aerogel, is a very low density chemically inert material with low thermal conductivity, excellent acoustic insulation properties and a highly interconnected porosity. These properties would render aerogels very desirable for numerous applications, but they have one serious drawback that has prevented their wide industrial, commercial and aerospace use: they are fragile materials, and thus they have seen only very limited use in specialized applications, for example as Cherenkov radiation detectors in certain types of nuclear reactors [4], in the Stardust program for capturing hypervelocity particles in space [5], and for thermal insulation aboard certain short-lived planetary vehicles such as the Sojourner Rover on Mars in 1997 [6]. Meanwhile, all future space Exploration Systems Research and Technology will rely decisively on weight reduction and multifunctional materials. Thus, if the excellent thermal insulating properties of aerogels can be combined with mechanical strength, aerogels will be ideal dual-function materials in this endeavor.

Aerogels are porous materials derived via a sol-gel process in combination with a subsequent drying step; the results are monolithic, open, porous materials with a backbone morphology that can be modeled in terms of three dimensionally interconnected strings of pearls. One of the significant advantages of aerogels compared to other porous materials is that both porosity and inner surface area can be tuned

independently. Porosities of up to 99.9 % are achievable; when micro porosity (IUPAC definition: pores < 2nm) is present, the specific surface area (BET) can exceed 1500 $m^2/g$. The length scale of both the "pearls" as well as the interconnected voids can be independently tailored over a wide range, i.e. from a few nanometers to several microns

The combination of such an extensive range of unusual material properties enables the application of aerogels in many different areas of technology. Some of these areas are presented in Figure 1

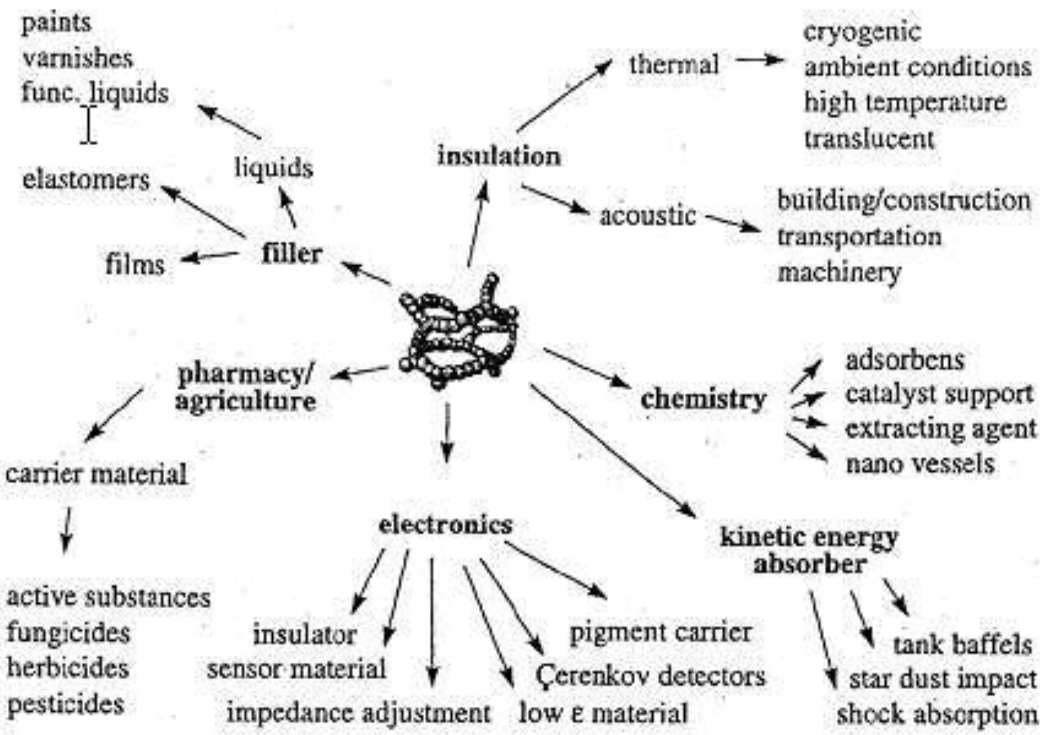


**Figure 1 Applications of aerogel in various fields Reference: [7]**

## 1.1 Thesis Outline

In Chapter 1, an introduction to nanostructured materials is presented. Chapter 2 is a literature review of work done previously by other researchers on testing and modeling of aerogels. Chapter 3 describes the procedures for preparation of monolithic crosslinked silica aerogel. Chapter 4 presents the experimental procedures used in characterization of silica aerogel. Chapter 5 describes the steps involved in modeling of aerogel. It explains the structure of silica aerogel, the diffusion limited cluster aggregation algorithm for generating the structure of the silica aerogel and the particle flow code (PFC3D) theory. Chapter 6 discusses results obtained from characterization tests and numerical modeling. Chapter 7 lists the conclusions based on the current study and discusses the scope for future study.

# CHAPTER 2

# LITERATURE SURVEY

Silica aerogels are brittle materials like glasses or ceramics. Their mechanical strength is very poor (less than 1 MPa) owing to their large pore volume. Nevertheless, knowledge of their mechanical properties is of interest for technical applications (Cherenkov detector, thermal insulator, host matrix) as well as for theoretical research. Many researchers have used different techniques for tailoring the properties of silica aerogel for specific applications. Experimental as well as simulations and analytical studies have been performed.

Woigner et al [8] conducted three-point bend and diametral compression tests on silica aerogel samples. The aerogels were obtained from tetramethoxysilane (TMOS), by hypercritical evacuation of the solvent. The stress-strain curve obtained showed a perfectly elastic behavior and "conchoidal" fracture morphology Based on the fracture morphology the material was predicted to be as brittle as a conventional glass. The bending strength ($\sigma_B$) of aerogels was found to be greater than the corresponding strength in diametral compression ($\sigma_{DC}$) with $\sigma_B/\sigma_{DC}$ ratio approximately equal to two. The

mechanical strength of aerogel was observed to be function of the bulk density; aerogels with the highest density (400 kg/m$^3$) revealing maximum flexural strength of 1 MPa.

Parmenter et al [9] investigated the mechanical behavior of silica aerogel using hardness, compression, tension and shear tests. The influences of testing conditions, storage environment and age were examined, with particular attention paid to the effects of processing parameters, including fiber-reinforcement. Good correlation was found between hardness and compressive strength over a wide range of processing parameters. Increasing fiber reinforcement generally retarded shrinkage during fabrication and yielded smaller matrix densities for a given target density. For a given fiber content, hardness, compressive strength and elastic moduli increased and strain at fracture decreased with increasing matrix density. In the lower ranges of matrix density, fiber reinforcement increased strain at fracture and elastic moduli. The mechanical response was also sensitive to environment and storage history. With age, the compressive strength and elastic moduli increased, while the strain at fracture decreased. Tension and shear results indicate that shear strength of aerogels exceeds tensile strength, which is consistent with brittle materials' response.

Takahashi et al [10] investigated the bending strength of silica aerogel with bimodal pores. Silica gels with both macropores and mesopores were prepared from water glass by fixing the transitional structure of phase separation. The bending strength was investigated, at different calcination temperatures and ammonia concentrations in aging, by conducting three-point bend test on rectangular specimens. The strength was seen to

increase with increasing calcination temperatures and with decreasing ammonia concentrations. Strong correlation was found between bending strength and mesopore volume. The bending strength was seen to be monotonically decreasing with increasing mesopore volume, as long as the gel had similar macroporous morphology. However, little correlation was observed between strength and structural parameters (such as pore diameter) of mesopores. The strength of the bimodal porous silica aerogel was predicted to be greater than that reported in the literature for silica aerogel with a similar porosity.

Martinez et al [11] investigated the response of silica aerogel to deformation by conducting microindentation. Mechanical properties such as hardness, Young's modulus and elastic parameter were obtained by microindentation measurements carried out on a Nanotest 550 (Micro Materials) Indenter. The effects of alkoxide concentration, solvent, drying procedure and carbon addition on mechanical properties were studied. The maximum applied load was 1mN and the maximum penetration depths were in the range 2-7 μm with resolution better than 1μN and 1 nm, respectively. With increase in alkoxide concentration, the density of aerogel increased, as did the hardness and Young's modulus. The effect of solvent was studied by using two different solvents, acetone (sample A) and methanol (sample B), to yield samples of similar densities. Sample B was seen to be more elastic than sample A, resulting in higher Young's modulus and lower elastic parameter as compared to sample A. The effect of drying procedure was studied by employing two different drying procedures, conventional high temperature supercritical extraction of acetone (sample X) and exchange of the acetone for carbon dioxide (sample Y). Shrinkage in sample Y was more pronounced, with sample Y being

harder and stiffer as compared to sample X. The effect of addition of small amount of activated carbon to the sol had a pronounced effect on the Young's modulus of aerogel. A marked change was observed in the nature of load vs. penetration depth curves, as they changed their trend from that of elastoplastic materials to highly elastic materials.

Martin et al [12] investigated mechanical and acoustical properties of macroporous silica aerogels as a function of polyethylene glycol (PEG) concentration. Young's modulus of silica aerogel was determined under uniaxial compression test and acoustical techniques. Mechanical properties, such as elastic coefficients, have been related to acoustic velocity using experimentally matched scaling laws. From both tests, they were able to get good correlation for the Young's modulus. The properties exhibited a large change when a small concentration of PEG was added to the initial sol. The stress-strain curve showed an initial linear elastic region, followed by a smooth transition to plastic region. They loaded the sample to 75% of its elastic limit and unloaded it to zero, three times and then loaded it to approximately 150% of its elastic limit to examine the linear recoverability of the silica aerogel. Beyond the elastic limit, the aerogel followed a different unloading curve due to permanent deformation.

The sub-critical crack growth domain in hydrophilic silica aerogel was studied using the Double-Cleavage-Drilled-Compression test (DCDC) [13]. The effects of temperature and water vapor content on the crack growth rate were measured. The experiments were carried out between 295 ˚K and 383 ˚K with air moisture ranging from 5 % to 80 % RH. Like dense silica, crack growth velocities were found to decrease when increasing the temperature at a constant water vapor concentration. Surprisingly, the crack velocity also

decreased with increasing water vapor content at constant temperature. Such a behavior is contrary to the expected results usually encountered in glasses. An analogy with nitrogen adsorption experiments on the same aerogels was used to explain this behavior. It was assumed that a capillary condensation phenomenon of water vapor inside the aerogel porosity occurred, inducing internal compressive stresses

Isostatic compression of silica aerogels is known to allow densification of these highly porous aerogel materials. However, at the onset of compression, hydrophobic and consequently slightly reacting aerogels exhibit a decrease in bulk modulus, as reported by Perin et al. [14]. This unusual behavior is associated with damage occurring at low pressures, which recovers with further increase in densification. Damage development and healing were analyzed measuring elastic modulus and, for the first time, internal friction as a function of compression. It was proposed that the origin of damage and healing could be associated with the rupture of tenuous links between clusters of dense silica particles at low density levels, and with the creation of new links between the resulting arms and reacting species that are revealed at cluster interface under higher pressure. It was also reported that a peak occurs in the internal friction of the aerogel at around 5 MPa pressure, indicating good damping characteristics under blast and/or impact loading.

Scherer et al [15] studied the compression of aerogel using mercury porosimetry. When aerogel was pressurized in a mercury porosimeter, the network got compressed, but no mercury entered the pores. Thus, porosimetry was employed to provide a measure of the

bulk modulus of the network. They observed that the silica aerogel, was linearly elastic under small strains, and then exhibited yielding followed by densification and plastic hardening. Power law relationships were fitted in linear elastic and plastic regimes. In the plastic regime, it was found that the bulk modulus has a power-law dependence on density with an exponent of 3.2. For the same gels, the linear elastic modulus (before compression) also obeyed a power law, but the exponent is = 3.6. If the aerogel is compressed to a pressure, $P_1$, that exceeds its yield stress, and then returned to ambient pressure, the plastic deformation is irreversible; if the same aerogel is then compressed to pressure $P_2$ ($P_2$ is greater than $P_1$), it behaves elastically up to $P_1$, then yields and follows the same power-law curve.

Miner et al [16] studied the effect of humidity on Young's modulus and non-recoverable strain for hygroscopic silica aerogel. The samples were tested in a controlled humidity chamber with the RH varied from 32% to 70%, beyond which the samples failed catastrophically. The mass gains over the desiccated condition varied from 4% at 32%RH to 12% for 70% RH. There was a slight increase in Young's modulus from 0.51 to 0.70 MPa and the non-recoverable strain increased from 0.047 to 0.059 over the studied humidity range. The yield stress did not show a significant change.

Gross et al [17] investigated the mechanical behavior of silica aerogels using ultrasonic and static compression experiments. The frequency employed for ultrasonic experiments was varied from 50kHz to 1 MHz. The mechanical behavior was investigated in this frequency domain as a function of internal and external gas pressure. The measurement of longitudinal and transverse sound velocities allowed the Young's modulus and

Poisson's ratio for aerogels of different densities to be determined upon the variation of internal and external pressures. From static compression tests it was determined that the low density aerogel display creep with a time constant of about 45 min.

The mechanical structure-property relationship of high-porosity materials, such as aerogels is not well understood. Modeling of mechanical the structure-property relationship for silica aerogel has been attempted by researchers [18, 19]. It has been shown that low-density aerogel materials exhibit a scaling relationship between their elastic modulus (E) and density ($\rho$) according to the relation $E \propto \rho^m$, where m is the scaling exponent. Typically the value of m for aerogels is greater than 2, which means that porous aerogels are orders of magnitude more compliant than their solid components. The general consensus is that there exists dangling mass – branches that hang off the main backbone of the network and do not bear load, and therefore the exponent is raised above 2. There are some qualitative explanations for the large m, including the effect of small neck-to-particle ratio, tortuosity cleavage of bonds under stress and reformation of new bonds. Unfortunately, a systematic study linking the scaling relationship to the microstructure of the gel network has not been conducted for crosslinked silica aerogel. The problem is that the elastic properties are controlled by the connectivity of the network, and there are no good experimental tools for measuring or quantifying it. Consequently, computer simulation is the most feasible approach to understanding the mechanical structure-property relationship of aerogels.

Gavalda et al [20] presented a molecular model for carbon aerogel. The aerogel studied in their work was mesoporous and had carbon particles having a diameter of ~6 nm, connected in an open-cell structure with a porosity of ~0.55. This structure was prepared by first generating a random close-packed structure of slightly overlapping spheres, followed by random removal of spheres to match the targeted porosity. Structural characteristics of the model have been studied using different Monte Carlo (MC) techniques and they compare well with those for the laboratory material. Nitrogen adsorption in their aerogel model was studied using a parallelized Grand Canonical Monte Carlo algorithm based on a domain-decomposition scheme. Adsorption occurs in the micropores at very low pressure, followed by adsorption in the mesopores, with capillary condensation occurring at the higher pressures.

# CHAPTER 3

# PROCESSING OF CROSSLINKED SILICA AEROGEL

Base-catalyzed silica aerogels consist of large voids called mesopores (~50 nm) in a "pearl necklace" of microporous secondary particles, as shown in Figure 2(a). These secondary particles are connected by "necks" formed by dissolution and reprecipitation of silica during aging. Consequently, it is reasonable to assume that the mechanical strength of monolithic aerogels can be improved by making the necks wider as shown in Figure 2(b). To accomplish this, the contour surface of the silica is used as a template for the deposition and growth of an inter-particle cross-linker.

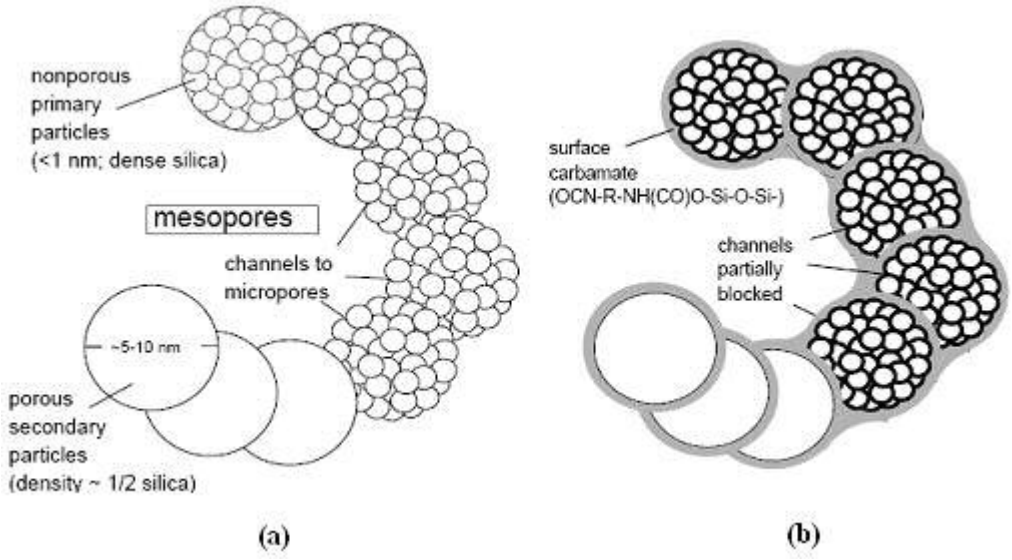


**Figure 2 Schematic diagram of aerogel (a) before and (b) after crosslinking. Reference: [21]**

There are, currently, a variety of methods for silica aerogel synthesis. The detail procedure used in preparation of silica aerogels in this study is described in the following paragraphs. (Synthesis method was developed by Leventis et al at NASA GRC [21])

The synthesis of aerogels, in general, involves two major steps, the formation of a wet gel, and the drying of the wet gel to form the aerogel. The preparation was wet gel was carried out at Oklahoma State University while, the drying of the wet gel was done at NASA Glenn research centre. The sol (sol is a solution of various reactants that are undergoing hydrolysis and condensations reactions) for the wet gels was prepared separately as two different solutions, namely solution "A" and solution "B". Solution "A" is a mixture of 1.3 ml aminoproplyltriethoxysilane (APTES), 6 ml acetonitrile ($CH_3CN$), and 3.85 ml tetramethoxysilane (TMOS), whereas solution "B" is a combination of 6 ml acetonitrile ($CH_3CN$) and 2 ml deionised water ($H_2O$). A mixture of dry ice and acetone was prepared and both the solutions were cooled separately in that mixture (mixture temperature –78 $^oC$) for about a minute. After cooling, solution "A" was poured into solution "B" and the mixture was agitated. The resulting sol was then poured into a mold of the desired shape. The mixture solidified in about a minute and the mold was covered with two layers of parafilm, to prevent the gel from drying. The sol was allowed to age in the mold till the gel point (the point at which the network of linked oxide particles span the container holding the sol) is reached. At the gel point, the sol forms a rigid substance called alcogel. The alcogel was gently removed from the mold and immediately transferred to a jar containing acetonitrile.

The acetonitrile in the jar was changed after a period of 24 hours for three days. After this period, the samples were removed from acetonitrile jars and were ready for crosslinking.

The alcogel samples were crosslinked with di-isocyanate (Desmodur N3200) as the crosslinker and acetonitrile as the crosslinking solvent. This is a critical step in the formation of crosslinked silica aerogel. A mixture of desmodur N3200 (32.9 gm) and acetonitrile (82ml) was prepared and vigorously shaken to ensure proper mixing to form a homogenous solution. The alcogel samples were then transferred carefully to the above mixture and allowed to equilibrate for 24 hours, with frequent agitation. At the end of the period, the samples were removed from the crosslinking bath and were placed in a container with fresh $CH_3CN$ and were placed in an oven (maintained at a temperature of $70^oC$) for 3 days. The samples were then removed and allowed to cool to room temperature, the crosslinking solution was decanted, and samples were washed four times with acetonitrile. The last major step in preparation of crosslinked silica aerogel, supercritical drying, was done at NASA Glenn research center. Supercritical drying is a process where the liquid within the gel is evaporated, leaving behind only the mesoporous silica network. The process is performed by prior solvent exchange with $CO_2$ followed by supercritical venting of the alcohol (lower temperatures-less dangerous). Figure 3 shows the schematic representation of the steps involved in preparation of silica aerogel.

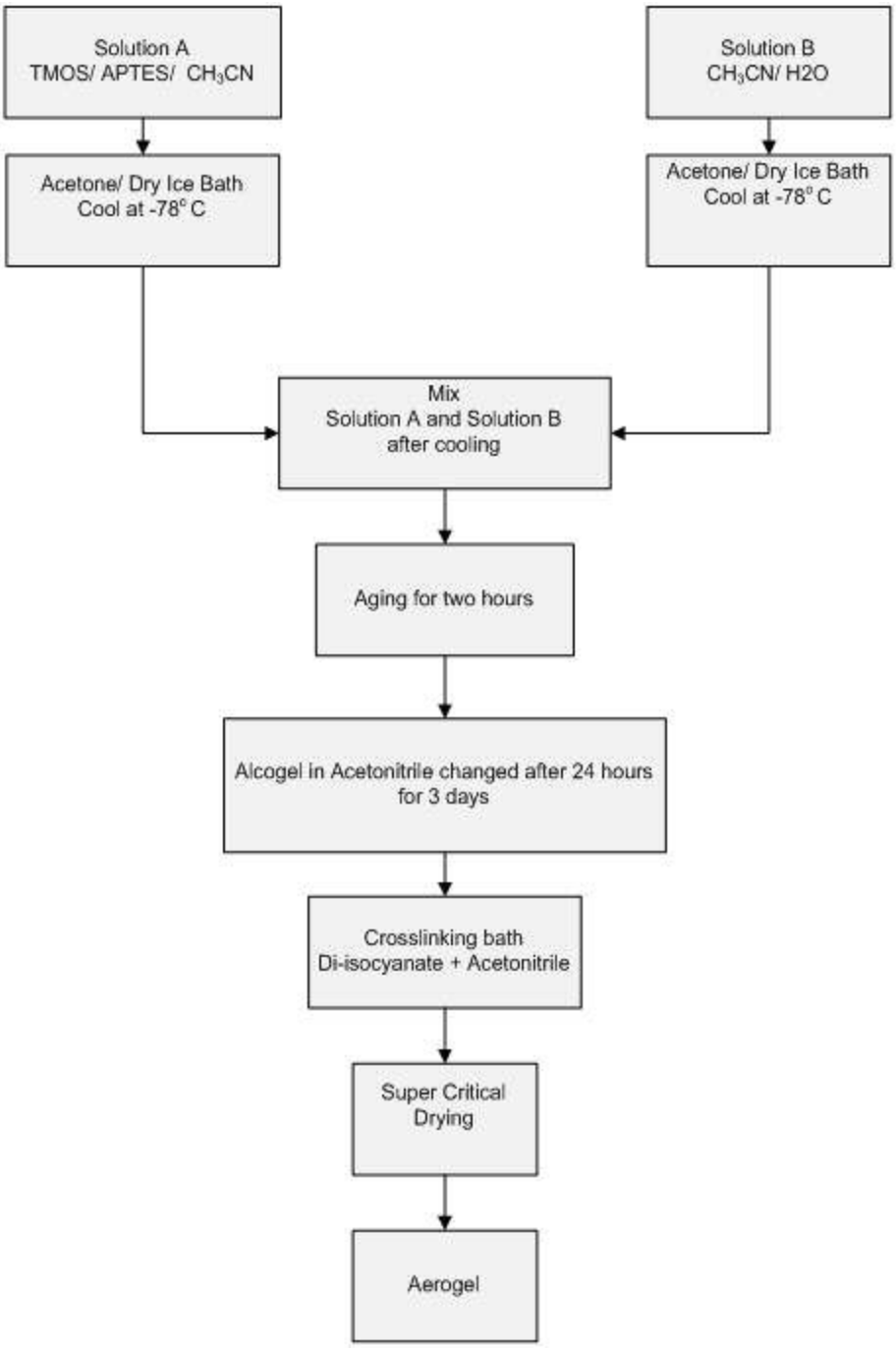


**Figure 3 Schematic representation of the synthesis of di-isocyanate crosslinked silica aerogel**

# CHAPTER 4

# MECHANICAL CHARACTERIZATION EXPERIMENTS

The aerogels prepared by the procedure described in Chapter 3 were characterized using different mechanical tests. The testing was carried out under different conditions to study their effects on the measured properties. Tests that were conducted are described as follows.

## 4.1 Compression Tests

Compression tests were performed on cylindrical cross-linked silica aerogel (CSA) specimens, on a MTS machine equipped with a 55,000 lbs load cell. Specimens with 2:1 height to diameter ratio were tested according to ASTM D790 standard. Five samples were each tested in uniaxial compression and their dimensions are tabulated in Table 1. The samples were sized at the ends using a 5200 rpm 10" compound power miter saw, followed by polishing of the cut surfaces on a fine belt grinder. The specimen was held between the platens of compression fixture, the top of which was held stationary whereas, the bottom platen was raised at the rate of 0.005inch/sec as shown in Figure 4. Solid graphite powder was used as a lubricant to reduce the friction between the platens and aerogel surface. The load and displacement data was recorded from Instron data acquisition console and was corrected for the machine compliance. Compression tests

were conducted at room temperature and lower temperatures of -27°C, -55 °C, and -196 °C. The samples were cooled in a freezer and liquid nitrogen dewar (Model B, Precision Cryogenics Systems, Inc, Indianapolis, IN) for 3 hours for tests conducted at -27 °C and -55 °C respectively. The samples were then removed from their respective coolers and immediately tested in air within a span of 2 minutes. For test at -196 °C, the samples were directly immersed in liquid nitrogen for 30 minutes and immediately tested on the compression fixture at room temperature. Since silica aerogels has a low thermal conductivity (0.03-0.04 W/m˚K) [22], it was anticipated that that there was not a large rise in the temperature of specimens during the test. The samples were tested within two minutes, after their removal from the liquid nitrogen.

The load-displacement curves were converted to stress-strain curves by dividing the loads by the original cross-sectional areas of the specimen, and the displacements by the original height of each specimen respectively. The compressive strength, the strain at failure and the Young's modulus values were extracted from the stress-strain curve. The strain at fracture is the strain at which the macroscopic failure of the specimen occurred. The influence of strain rate on compression of the samples was quantified by comparing the stress-strain curves at different strain rates. The samples were loaded at strains rates of 0.35 %, 3.5% and 35% per second.

The effect of aging on the mechanical properties was measured by evaluating stress-strain curves for aerogel specimens having different storage history. Some compression

specimens were tested within a week of manufacture; some were tested after being stored in air environment under ambient conditions for approximately 5 weeks.

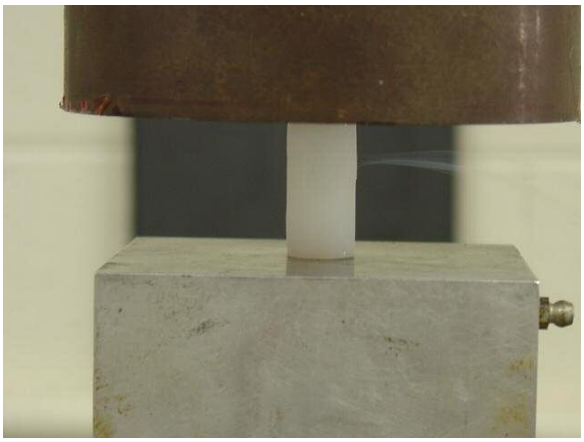

**Figure 4 Uniaxial compression testing setup**

### 4.2 Flexural Tests

Three-point bending tests were performed on rectangular samples, as shown in Figure 5, using an INSTRON 4240 servo-hydraulic machine equipped with a 100 lb load cell and a PID servo controller. The crosshead speed was 2.54 mm/min and the fulcrums span was 50mm. The tests were conducted at room temperature (21°C). The load and displacement readings were acquired using the NI LabView data acquisition software. The stress readings were calculated from the load readings using the flexural formula $\sigma = My/I$ and the strain was measured at the bottom-most point using a relation derived from total strain energy principle, taking shear deformation into account. The bending stiffness and the bending strain at failure were determined from the stress-strain curve. The effect of temperature on silica aerogel bending strength was quantified by comparing stress-strain curves at room temperature (21°C), –196°C and 180°C. For the tests at -196°C, the samples were directly immersed in liquid nitrogen for 10 minutes and tested within two minutes, after they were removed from liquid nitrogen, on the bending fixture at room

temperature. As mentioned earlier, it was assumed that there was not a significant rise in the temperature of specimens during the test.

The tests at 180°C were conducted on the bending fixture inside an Instron environmental chamber. Three samples were soaked at 180°C for six hours to ensure that thermal equilibrium has been reached. There was shrinkage in the sample dimensions and the surface morphology changed to a glassy material as shown in Figure 6. The dimensions of the samples and load-deflection curves are discussed in dicussion section

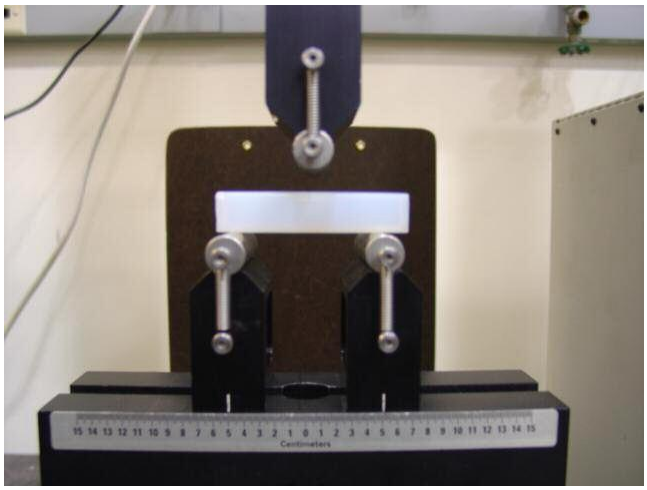

**Figure 5 Flexural testing setup**

**Figure 6 Sample shrinkage and change in surface morphology of CSA sample at -180C**

# CHAPTER 5

# MECHANICAL STRUCTURE-PROPERTY RELATIONSHIP OF SILICA AEROGEL

In this chapter, the steps involved in development of the numerical model are explained. Firstly, the structure of silica aerogel, as investigated from different characterizing techniques, is presented. Secondly, the diffusion limited cluster-cluster aggregation (DLCA) algorithm, used in the generation of the aerogel structure is described. Thirdly, the outlying theory of particle flow code and the process of numerical modeling are described.

## 5.1 Structure of silica aerogel:

Aerogel is a class of monolithic materials that possesses porous structure. The mechanical, thermal, electrical and optical properties exhibited by aerogels are attributed to their nanoporous cluster assemblies. As previously mentioned the properties of aerogel, such as Young's modulus are directly related to their structural parameters. Therefore, it's of prime importance to investigate the micro-structural features of aerogels. Various research groups are actively engaged in revealing the complex structural feature of this highly compliant material.

Scanning electron microscopy (SEM) [23] and transmission electron microscopy (TEM) [24] have been employed to produce a direct image of the nanoporous aerogel structure. Indirect imaging techniques, such as small angle x-ray scattering (SAXS) [25] and small angle neutron scattering (SANS) [26], are widely used to reveal the structural features of aerogels. Nuclear magnetic resonance spectroscopy (NMR) has also been used to examine the structural evolution of aerogels on the molecular level [27].A laser ablation technique, using time of flight method, was used by one such group to reveal the structure of aerogel [28]. The schematic sketch of their proposed aerogel structure is shown in Figure 7. For the crosslinked silica aerogel used in the present study, SEM imaging was conducted at Ohio aerospace institute and the structure under different magnifications is shown in Figure 8. In the figure, the clusters of secondary particles are clearly visible along with the nanopores.

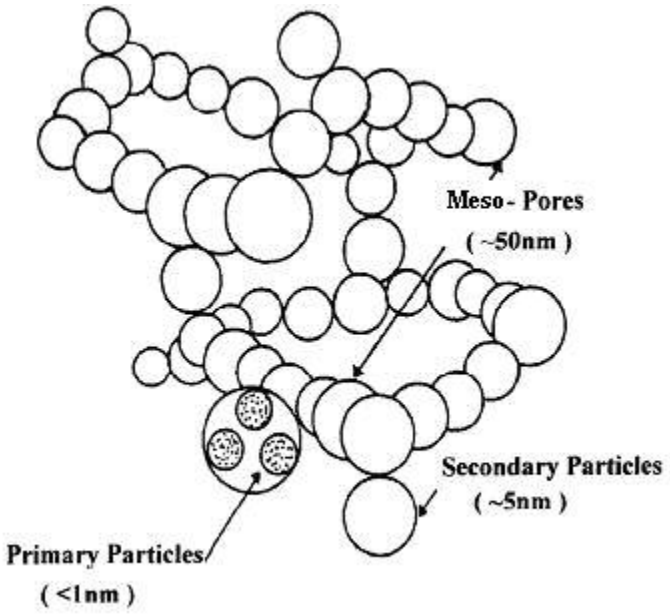


**Figure 7 Schematic of silica aerogel structure as determined from laser ablation technique [Ref: 28]**

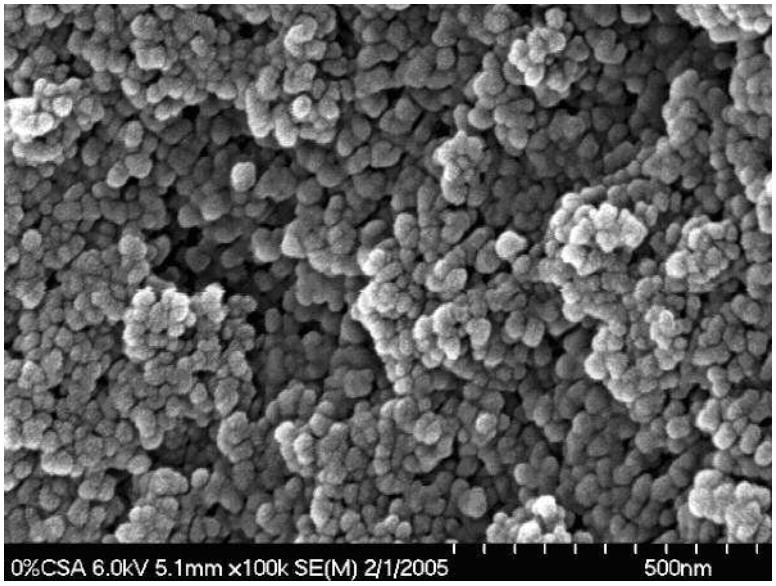


**(a)**

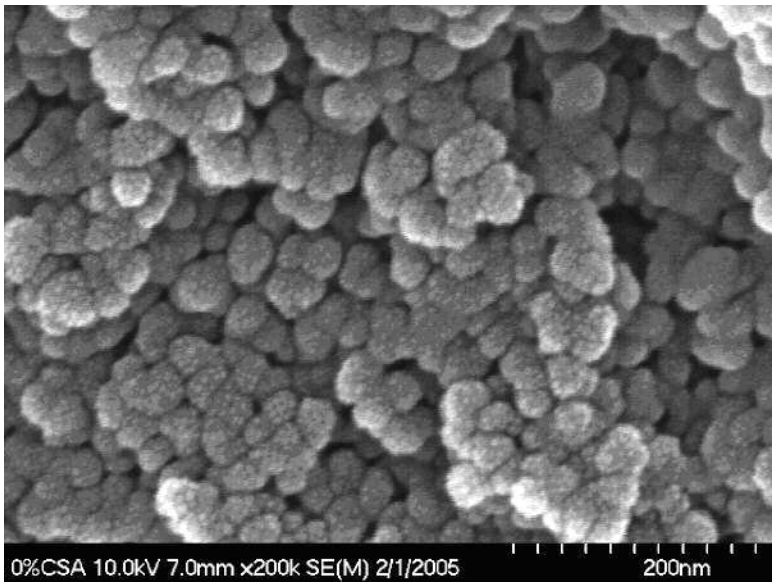


**(b)**

**Figure 8 SEM images of crosslinked silica aerogels. The cluster of secondary particles (round particles) and the mesopore (dark spots) are clearly visible.**

**(Courtesy -Ohio Aerospace Institute)**

**(a) 500 nm magnification (b) 200 nm magnification**

The stiffer structure exhibited by aerogel depends on the connectivity of its network of particles in space. However, there is no experimental technique to measure the connectivity of the particles. Various researchers have developed different cluster aggregation algorithms for simulating the growth of aerogels such as diffusion limited cluster algorithm, reaction limited cluster algorithm [29, 30]. A diffusion limited cluster aggregation algorithm has been used in present study, as it is simple to implement and well characterized. It was developed to aid the interpretation of scattering experiments and subsequently has been employed to aid the understanding of phenomena related to porous media such as gelation, fractal studies, scattering spectroscopy.

### 5.2 **Description of the DLCA algorithm**

The DLCA algorithm proceeds with random filling of non-intersecting spheres inside a cubic volume. The diameters of these spheres are chosen from a Gaussian distribution function. These spheres are then set to diffuse inside the cubic boundary. When in motion, a particle (or cluster) is tested for overlap with neighboring particles. If an overlap is detected, then that particle is merged to the particle or cluster. The diffusive motion is completed once all the particles have merged to form a single cluster [30]. The process of aggregation is schematically explained in Figure 9. A cluster of three particles is moved and is tested for an overlap with neighboring particles as shown in Figure 9 (a). Once an overlap is detected this cluster is aligned to the particle as shown in Figure 9 (b). Then, this cluster and particle are merged to form a cluster with four particles as shown in Figure 9 (c). This process continues until all particles have merged to form a cluster. Figure 10 shows snapshots of the DLCA process developed using POV ray (persistence

of vision) software. 13800 particles are dispersed in a cubic volume of 400 nm in each dimension. Figure 10(a) shows the cubic volume filled with random non-intersecting spheres. These spheres put in Brownian motion. Figure 10(b) shows the spheres merged together to form a single cluster.

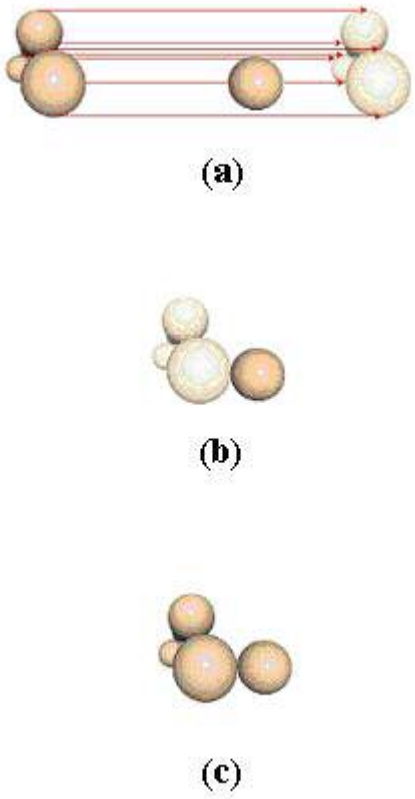


**Figure 9 Process of aggregation of the particles [Ref: 31]**

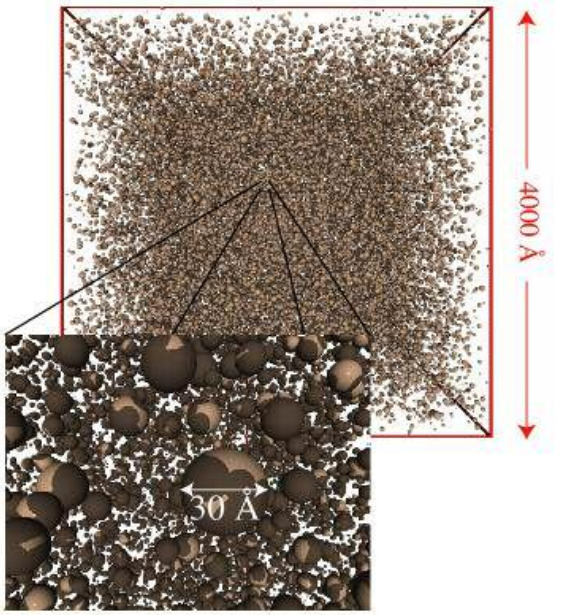


(a)

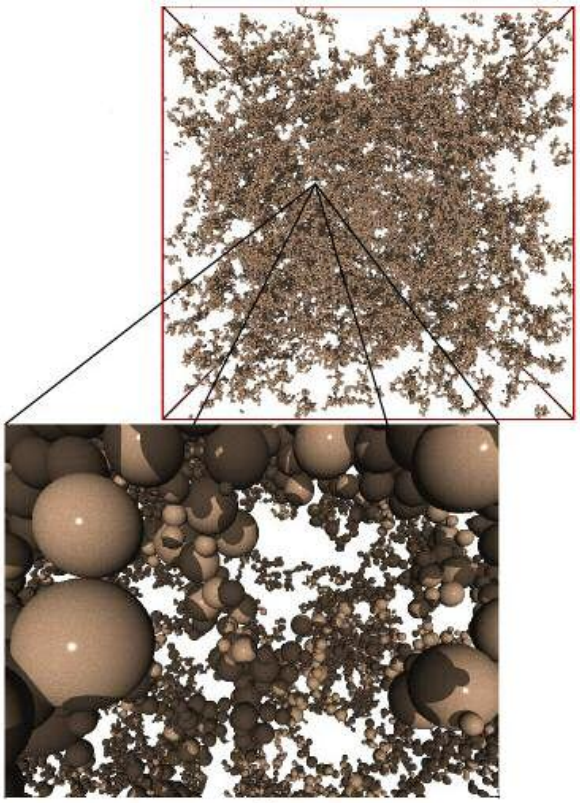

(b)

**Figure 10 (a) Non-intersecting spheres dispersed in a cubic volume (b) spheres put in diffusive motion to form cluster after the aggregation process [Ref: 31]**

### 5.3 Particle Flow Theory

A Particle Flow Code in three dimensions ($PFC^{3D}$) models mechanical behavior by representing a solid as a bonded assembly of spherical particles. The modeling process is based on discrete element (also called distinct-element) theory. PFC models are categorized as direct, damage-type numerical models in which the deformation is not a function of prescribed relationships between stresses and strains, but of changing microstructure. The following sections describe general principles of the particle mechanics approach and the distinct element method and are based on PFC manuals published by Itasca (1999) [32].

#### 5.3.1 Particle mechanics

PFC3D (Particle Flow Code in 3 Dimensions) is program for modeling the movement and interaction of assemblies of arbitrarily sized spherical (3D) particles. The model is composed of distinct particles that displace independently from one another and interact only at contacts between the particles. Newton's laws of motion provide the fundamental relationship between particle motion and the forces causing the motion. Bonding the particles together at their contact points, and allowing the bond to break when the strength limit of the bond is exceeded, can model behavior that is more complex. In addition to spherical particles, i.e. balls, the PFC model also includes 'walls'. The desired model is constructed from these two entities.

### 5.3.2 Distinct Element Method

PFC models the movement and interaction of particles using the distinct element method (DEM). PFC is classified as a discrete element code because it allows finite displacements and rotations of discrete bodies and because it recognizes new contacts automatically. The program is a simplified implementation of the distinct element method because of the restriction to rigid spherical particles. In PFC, interactions between particles are treated as a dynamic process. Dynamic behavior in PFC is represented in numerical terms by a time-stepping algorithm which requires repeated application of the laws of motion to each particle, a force-displacement law to each point of contact, and a constant updating of wall position. The use of an explicit numerical scheme makes it possible to simulate the nonlinear interaction of a large number of particles, without the requirement for the computer equipment being used to have extensive memory.

### 5.3.3 Calculation cycle

The PFC calculation cycle is shown in Figure 11. At the start of each time step, the set of contacts is updated from the known particle and wall positions. The force displacement law is then applied to each contact to update the contact forces, and the law of motion is then applied to each particle to update its velocity and position.

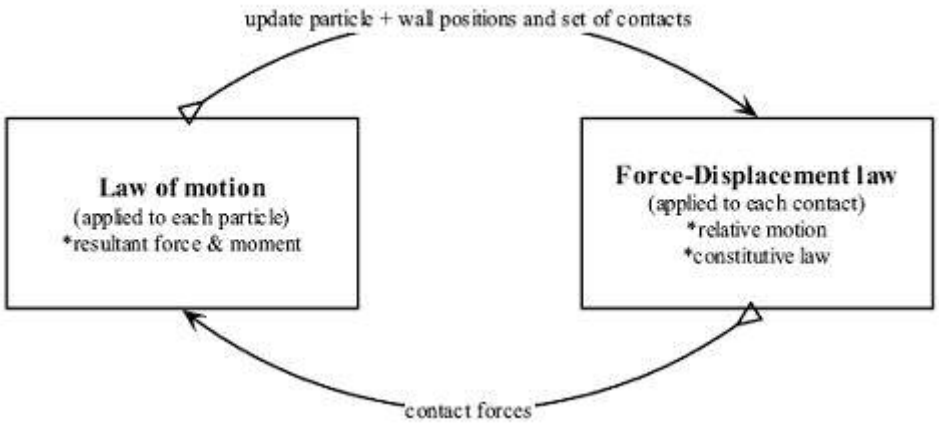


**Figure 11 Calculation cycle in PFC3D; Reference [32]**

### 5.3.4 Contact models

A contact model describes physical behavior at each contact. The constitutive model acting at a contact consists of a stiffness model, a slip model or a bonding model as shown in Figure 12. The stiffness model is an elastic relationship between force and displacement. The slip model introduces friction into contact behavior. Particles may also be bonded together at a contact (the bonding model). Two bonding models are supported in PFC. Both bonds can be described as the 'gluing together' of two particles. The contact-bond glue is of vanishingly small size and acts only at the contact point. The parallel-bond glue has a finite size and acts over a circular cross-section positioned between the particles.

A contact bond provides each contact point with a tensile normal and shear contact-force strength. This allows a tensile force to develop between two particles. If the magnitude of the tensile normal or shear contact force exceeds the respective strength, the bond breaks. Two particles with a contact bond behave as though they are welded together at the

contact point; thus, no slip is possible while the bond remains intact. However a contact bond provides no resistance to rolling. Rolling is caused by an unbalanced moment acting at the contact point. The difference between the bonding models is that while the contact bond can only transmit a force, the parallel bond can also transmit moment.

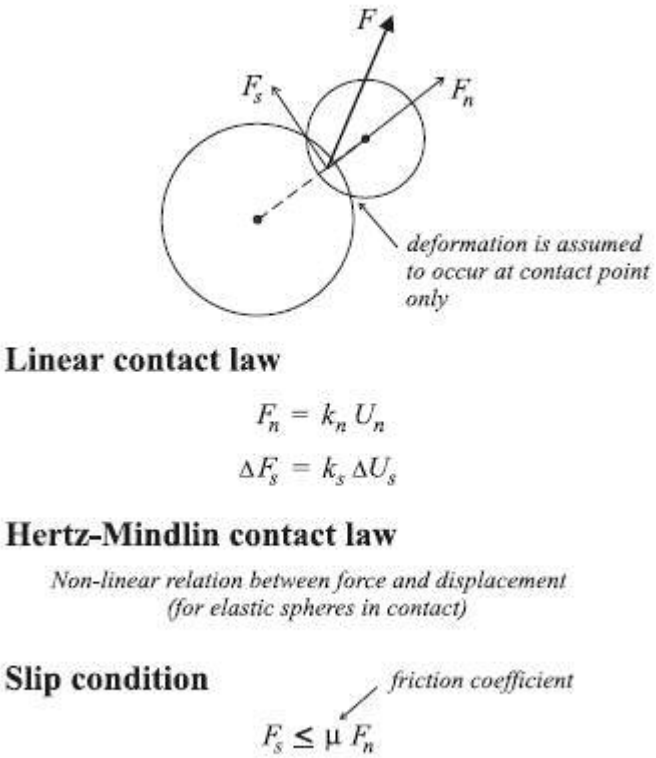


**Figure 12 Types of contact models in PFC3D; Reference [32]**

### 5.3.5 Choosing material properties for PFC3D models

In a general sense, one can characterize any model of a synthetic material by the parameters of deformability and strength. In order to have confidence that a particular model is reproducing desired physical behavior, it is necessary to relate each model

parameter to a set of relevant material properties. In the case of the PFC model, the model parameters cannot, in general, be related directly to a set of relevant material properties because the behavior of the PFC model is also affected by particle size and packing arrangement. The relation between PFC model parameters and commonly measured material properties is only known *a priori* for certain simple packing arrangements. For the general case of arbitrary packing of arbitrarily-sized particles, the relation is found by means of a calibration process in which a particular instance of a PFC model, with a particular packing arrangement and set of model parameters, is used to simulate a set of material tests (e.g., unconfined compression test, triaxial test, Brazilian test). The PFC model parameters are then chosen to reproduce the relevant material properties as measured in such tests.

### 5.3.6 Relation between Macro and Micro Properties

In order to create a synthetic material that exhibits a set of macroscopic responses that are independent of particle size, one must set the micro-properties of the PFC model using the relations described in this section. The micro-property-specification procedure requires relating the deformability and strength micro-parameters (particle and bond stiffnesses, particle friction coefficients and bond strengths) to their corresponding set of macro-responses (such as elastic constants, material friction angle and peak-strength envelope). The relations at the level of a single particle-particle contact are described subsequently by comparing either the behavior of a bond between two particles (for bonded material) or of the contact itself (for unbonded material) to that of an elastic beam with its ends at the particle centers. These relations provide a coherent set of micro-

parameters that can be determined for a particular physical material by carrying out the calibration process. A flow chart for the calibration process is shown in Figure 14.

All of the following analyses relate the behavior of a contact between two particles to that of an elastic beam with its ends at the particle centers. The beam is loaded at its ends by the corresponding force and moment vectors acting at each particle center. The beam is characterized by geometric parameters of length (L), cross-sectional area (A) and moment of inertia (I); deformability parameters of Young's modulus (E) and Poisson's ratio (υ); and strength parameters of normal ($\sigma_C$) and shear ($\tau_C$) strengths. The Young's modulus of a particle-particle contact and a parallel bond are designated by *Ec* and *Ep*, respectively.

The particle contact stiffness, the contact coefficient of friction, and the contact bond model used between the individual particles govern the mechanical behavior of the intact material. PFC3D provides the following two equations that can be used to make first estimates of the particle stiffness and bond strength from values of the macro-mechanical parameters determined in laboratory experiments.

$$E = \frac{K_n}{4R} \quad \text{..... (1)}$$

where E is the expected Young's modulus of the particle assembly as obtained from laboratory tests, $K_n$ is the normal stiffness of the particles and R is the particle radius, and

$$\sigma_t = \frac{S_n}{4R^2} \quad \text{..... (2)}$$

where $\sigma_t$ is the measured tensile strength of the particle assembly and $S_n$ is the normal bond strength between the particle contacts. The shear components of the stiffness and bond strength, $K_s$ and $S_s$, are taken to be some fraction or equal to their respective normal components. The two relations are derived for a cubic array of particles, which may not be correct representations of the actual particle arrangement in the laboratory samples. Nevertheless, the equations do provide useful information that could be used in obtaining first estimates of the micro-mechanical parameters values. The first equation shows that the Young's modulus, a macro-mechanical property, is inversely related to the particle radii and directly related to the particle stiffness. The second equation shows an inverse square relation and a direct relation between the expected tensile strength of the particle assembly and the particle radii and normal bond strength, respectively.

### 5.3.7 Parallel-Bond Behavior

A parallel bond approximates the physical behavior of a cement-like substance lying between and joining the two bonded particles. Parallel bonds establish an elastic interaction between particles that acts in parallel with the slip or contact-bond constitutive models. A schematic idealization of parallel bond is showing in Figure 13.

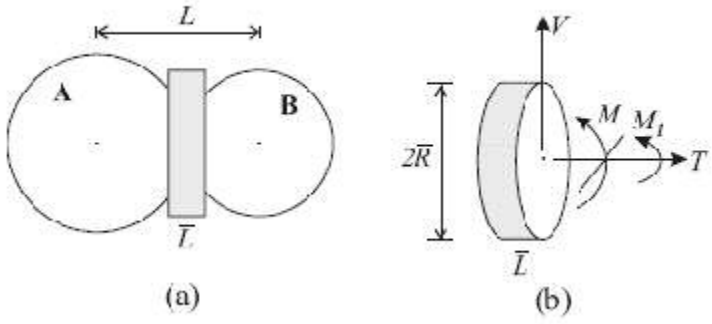


**Figure 13 Idealization of Parallel bond in PFC3D**

A parallel bond is defined by five parameters, namely the normal stiffness 'kn', shear stiffnesses 'ks', normal strength '$\sigma_C$', shear strength '$\tau_C$' and bond radius, R. When either '$\sigma$' or '$\tau$' exceeds the corresponding strength, the bond breaks.

The relation between the stiffnesses ($\overline{k^n}$) and the modulus ($E_P$) of the parallel-bond material are

$$\overline{k^n} = \frac{E_P}{L} \quad \text{..... (3)}$$

$$\sigma_C = \tau_C = S \quad \text{..... (4)}$$

where 'L' and 'S' are the bond length between the two particles in contact and the compressive strength of aerogel as determined from experiments respectively.

The values of parallel-bond normal and shear strengths, $\sigma_C$ and $\tau_C$, are specified in stress units. Thus, there is a direct one-to-one correspondence between parallel-bond strengths and material strengths. Recollect that a parallel bond can carry load in bending. The bending strength does not enter directly into the parallel-bond formulation. Instead, bending load contributes to the maximum fiber stress carried by the bond, and can thus induce a normal-mode failure. The bending-load contribution scales as bond radius.

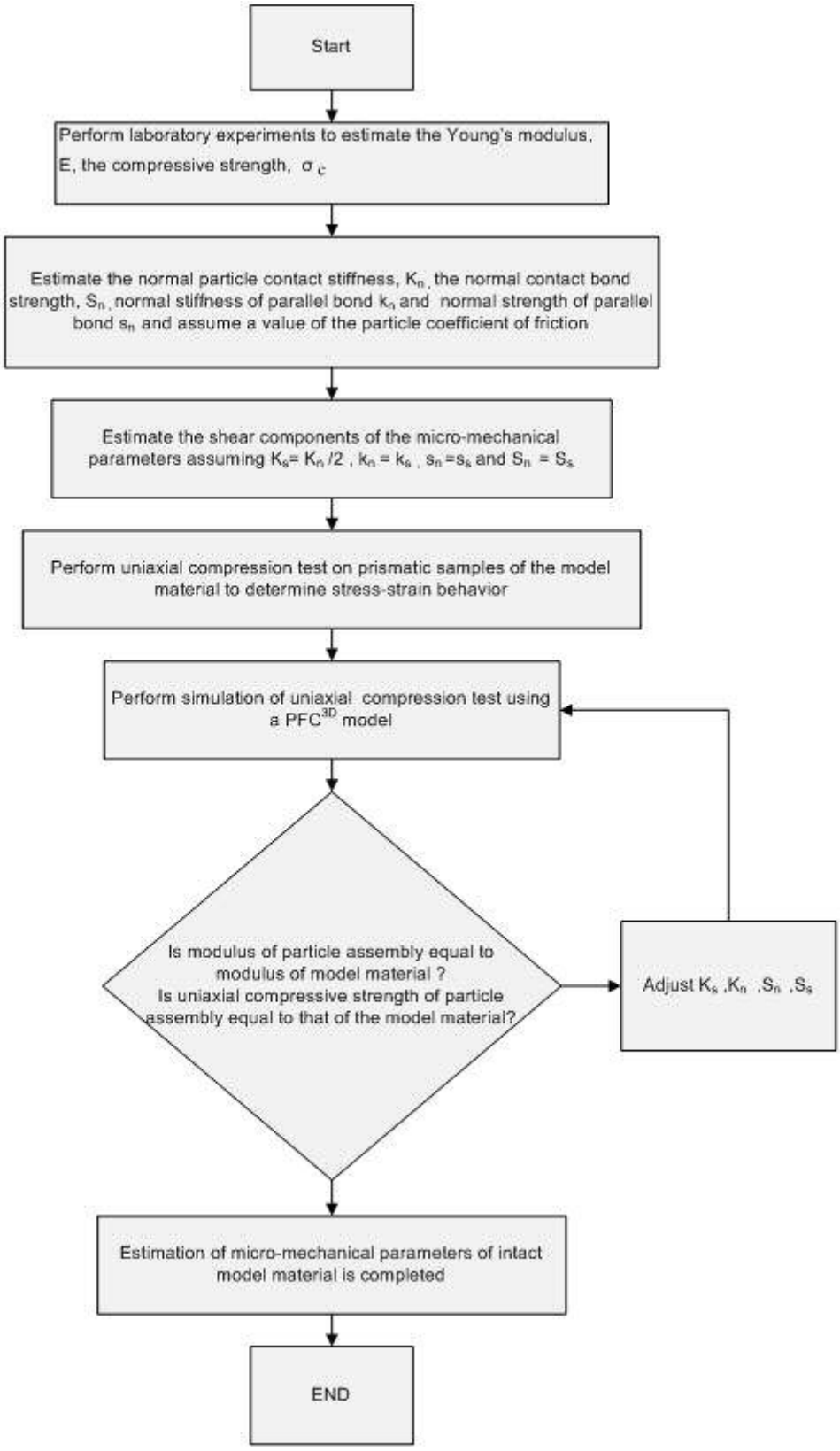


**Figure 14 Flow chart of the numerical modeling process**

# CHAPTER 6

# RESULTS AND DISCUSSION

## 6.1 Uniaxial Compression

Uniaxial compression experiments were conducted on crosslinked silica aerogel. A strain rate of $0.0035s^{-1}$ was used in all compression tests. Figure 15 shows the average stress-strain data for crosslinked silica aerogel specimens under compressive loading at room temperature. Data for individual samples, and average values with their standard deviations are summarized in Table 1. The compressive strength data for plain silica aerogels are given in Table 2 for comparison.

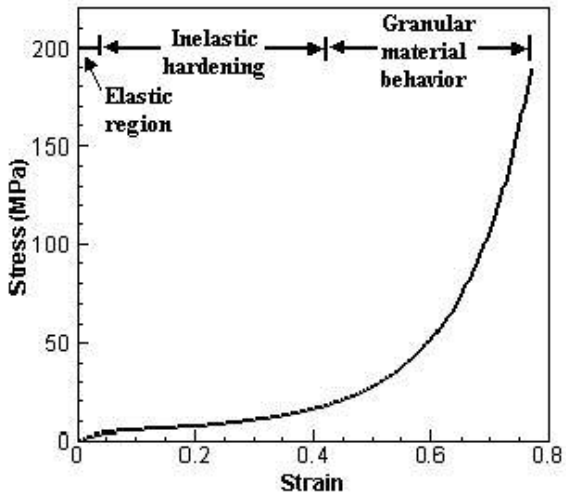


**Figure 15 Stress-strain curve in unaxial compression on crosslinked silica aerogel**

| *Sample Number* | *Density (gm/cc)* | *Compressive Strength (MPa)* | *Failure Strain (%)* | *Young's Modulus (MPa)* |
|---|---|---|---|---|
| 1 | 0.48 | 190.33 | 77.22 | 122.85 |
| 2 | 0.47 | 222.08 | 77.04 | 119.58 |
| 3 | 0.48 | 168.55 | 77.2 | 126.27 |
| 4 | 0.48 | 173.72 | 76.1 | 135.27 |
| 5 | 0.48 | 173.20 | 78.35 | 138.94 |
| Average | 0.478±0.004 | 185.58±22.02 | 77.18±0.78 | 128.58±8.23 |

**Table 1 Compressive strength data of isocyanate crosslinked silica aerogels.**

| *Sample Number* | *Density (gm/cc)* | *Compressive Strength (MPa)* | *Failure Strain (%)* | *Young's Modulus (MPa)* |
|---|---|---|---|---|
| 1 | 0.18 | 4.0 | 5.31 | 96.7 |
| 2 | 0.20 | 4.1 | 6.00 | 86.9 |
| Average | 0.190±0.014 | 4.1±0.07 | 5.66±0.49 | 91.8±6.9 |

**Table 2 Compressive strength data of plain silica aerogels.**

**Figure 16 Silica aerogel sample shattering into pieces at failure**

Figure 16 shows the snapshot of the crosslinked silica aerogel sample at failure. As seen from recorded images of sample at different stages of compression, the specimen did not exhibit significant lateral dilatation (the Poisson ratio is only 0.18) and did not buckle in compression. At failure, the outer layer of all samples shattered and fell away, while all

remaining cores, have the same height, indicating that failure is due ultimately to lateral tensile stresses even though the applied load is compressive. The average load at failure for the five specimens tested was 12065 lbs. Both the strain at failure and the compressive strength of the crosslinked silica aerogel are considerably higher than those of native (uncrosslinked) aerogels, which have a compressive strength of only 4.1±0.1 MPa. By comparison, crosslinking has increased failure strain by a factor of 13.5, and increased the compressive strength by a factor of 45. Nevertheless, assuming a power law dependence of the yield strength ($\sigma_s$) on density ($\rho$), $\sigma_s = \rho^{\alpha}$ it is calculated from the strength data of Tables 1 and 2 that $\alpha$=4.14.

Table 3 compares the absolute and specific compressive strengths of crosslinked aerogels with other materials. The specific compressive strength of crosslinked aerogels is higher than that of steel, aluminum 6061 T-6, fiberglass, and is comparable to that of aerospace grade graphite composite. The stress at which failure of the composites due to matrix failure or the yielding of metals occurred was used to compute the specific compressive strength.

| *Material* | *Density (g/cc)* | *Compressive Strength (Mpa)* | *Specific Compressive Strength (Nm/Kg)* |
|---|---|---|---|
| E-glass epoxy* | 1.94 | 550 | 283000 |
| Kevlar-49 epoxy* | 1.30 | 280 | 215000 |
| T 300 epoxy* | 1.47 | 830 | 564000 |
| VSB-32 epoxy* | 1.63 | 690 | 423000 |
| GY-70 epoxy* | 1.61 | 620 | 385000 |
| 2024 T3 Al | 2.87 | 345 | 120000 |
| 7075T6 | 2.80 | 475 | 169000 |
| 4130 steel | 7.84 | 1100 | 140000 |
| CSA | 0.48 | 186 | 389000 |

* Fiber volume fraction $V_f$=0.6

**Table 3 Comparison of specific compressive strength of crosslinked silica aerogels with various materials**

Young's modulus in compression was evaluated from the slope of the initial linear part (at <4% strain) of the stress-strain curve. The compressive Young's modulus of the crosslinked aerogel is 129±8 MPa compared to 92±7 MPa of the plain silica aerogel. But, the elastic part of the stress-strain curve has other similar characteristics with the stress-strain curve of the underlying native silica framework as well: it extends up to ~5 MPa and ~4% strain, while the native silica framework fails at 4.1±0.1 MPa and 5.7±0.9% strain. These data seem to suggest that at small strains the mechanical behavior of the composite material, at the specific silica to polymer ratio, is shaped by the stiffer silica framework, while at higher strains, the behavior of the material under compression is controlled by the porous polymer network. That realization should be reflected in the recovery (spring-back) behavior of the material during loading-unloading cycles along the stress-strain curve. Indeed, a typical cylindrical sample was loaded and unloaded six times, first in the elastic region where deformation is completely recovered as shown in Figure 17.

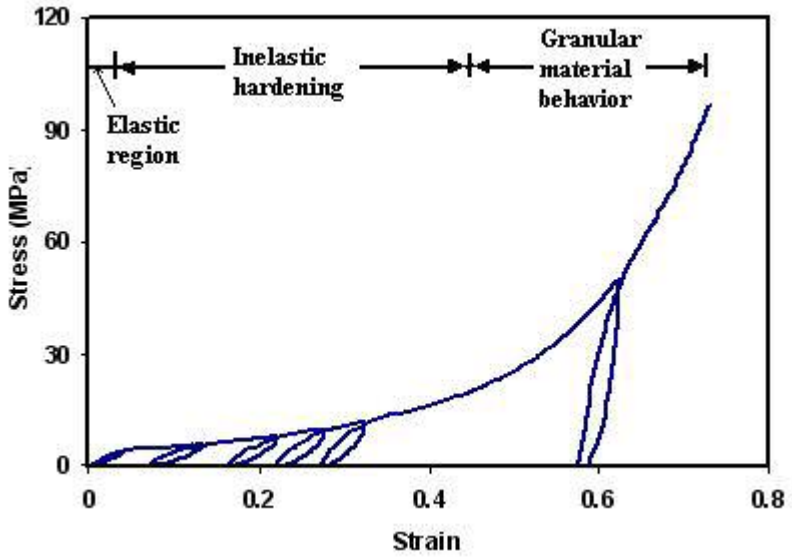


**Figure 17 Loading -unloading on crosslinked silica aerogel**

Then it was unloaded and reloaded in the plastic region where a hysteresis loop was always observed, presumably due to energy loss because of slipping of polymer chains. It is further noted that the percent strain recovery becomes progressively lower at higher strains, while in the inelastic hardening range (~60% strain) there is practically no strain recovery. Beyond 60% strain, the behavior is analogous to a granular material. The changes in the morphology of the material under compression were evaluated by SEM (Figure 18) and porosity/surface area analysis (Table 4). For this, samples were loaded up to a predetermined strain and subsequently the load was removed and the samples were analyzed. Curiously, under SEM, the material does not show any appreciable difference from its original state up to at least 45% strain. Surface area analysis, however, showed unambiguously that as the degree of plastic deformation increases, the surface area decreases and the average pore diameter increases, consistently with loss of mesoporosity as particles are squeezed closer to one another permanently. Ultimately, at failure (77% strain), the SEM shows clear signs of gradual collapse, i.e., a loss of porosity, which is supported by surface area analysis.

| Strain (%) | BET Surface Area ($m^2 g^{-1}$) | Average Pore Diameter (nm) |
|---|---|---|
| 0 | 261 | 9.7 |
| 30 | 197 | 15.2 |
| 45 | 152 | 169 |
| 77 | 6 | a |

a. low c-value (5.22)

**Table 4 Surface area analysis along compression of crosslinked silica aerogels (Courtesy- NASA GRC)**

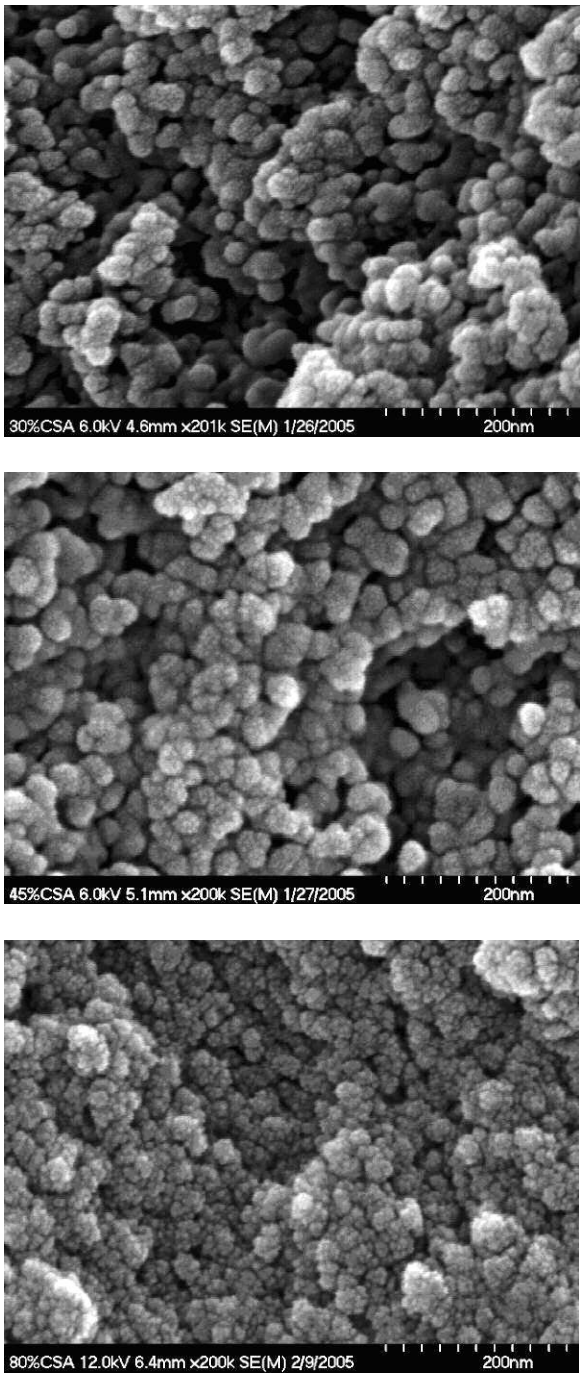


**Figure 18 SEM images of the morphological changes after compression in crosslinked silica aerogel specimen loaded at different percent strain**

**(a) 30% - No appreciable change in mesoporous structure**

**(b) 45% - Gradual decrease in the mesoporosity, few dark spots.**

**(c) 77% - Appreciable loss of porosity, particles are squeezed closer to one another**

Finally, the effects of the strain rate and temperature on the compressive strength were both evaluated. Figure 19 shows stress-strain curves at three compressive strain rates, $0.0035s^{-1}$, $0.035s^{-1}$ and $0.35s^{-1}$, tested at room temperature (21°C). The stress-strain curve at 0.0035 $s^{-1,}$ is an average for total of five specimen tested. For the tests at high strain rates, $0.035s^{-1}$ and $0.35s^{-1}$, two samples each were tested and the average curve was plotted. A good reproducibility of data at each strain rate was observed, with the maximum deviation of less than 1%. There was a gradual increase in Young's modulus, with an increase in strain rate. The Young's modulus data are 128MPa, 160MPa and 205MPa at strain rates $0.0035s^{-1}$, $0.035s^{-1}$, and $0.35s^{-1}$, respectively. The strain rate was varied by a factor of 100, yet the overall stress-strain curves did not change significantly, indicating that increased strain rate does not have a deleterious effect on the energy-absorption behavior of crosslinked aerogels under compression within the range of strain rates tested.

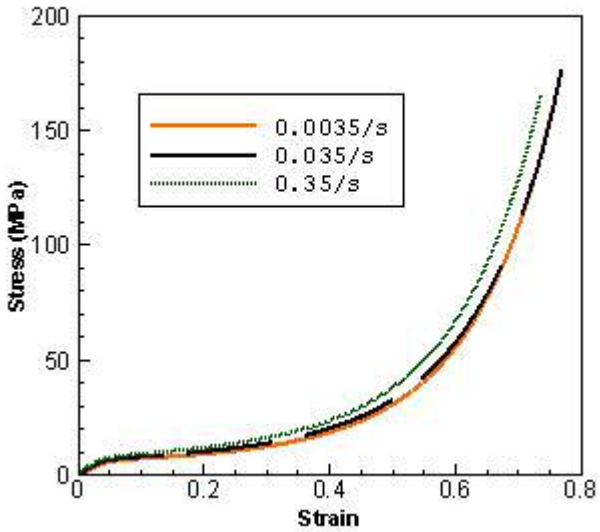


**Figure 19 Effect of strain rate on the behavior of crosslinked silica aerogel under uniaxial compression**

Figure 20 shows the stress-strain curves for crosslinked aerogel samples in compression testing at various temperatures. The mechanical response is essentially invariant of the temperature in the range between 21 ºC and –55 º. However, the material stiffens significantly (the elastic modulus increases to 450 MPa) and suffers premature compressive failure at cryogenic temperatures (e.g., –196 $^{o}$C).

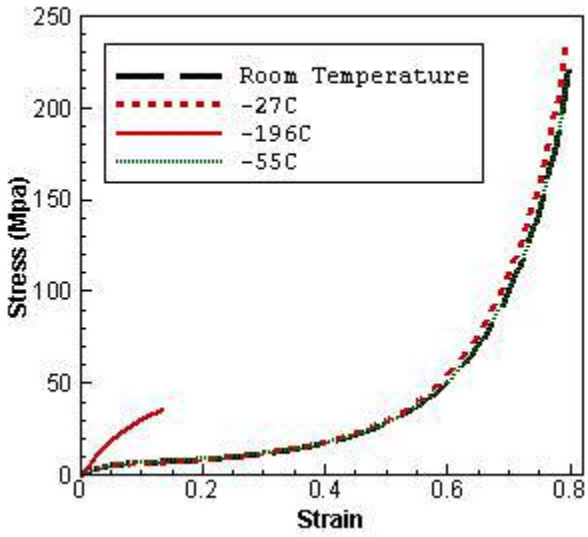


**Figure 20 Effect of temperature on the behavior of crosslinked silica aerogel under uniaxial compression**

### 6.2 Flexural Testing

Figure 21 shows the results for three-point bending tests. As the specimen length was small compared to the height of the specimen, shear deformation was taken into account in the load point deflection. The Young's modulus was calculated from the formula derived in Appendix A. The formula was derived from energy approach by considering both, bending as well as shear deformation. The modulus of Elasticity (E) was obtained from the formula for load point deflection, and is given as follows

$$E = \frac{PL^3}{48I\Delta}\left[1 + \frac{48(1+\nu)}{5}\left(\frac{h}{L}\right)^2\right] \quad \text{..... (5)}$$

Where, I is the area moment of inertia, P is the applied load, L is the length of beam span, $\Delta$ is the load-point deflection, $\nu$ is the Poisson's ratio and h is the thickness. Therefore, knowing the applied load, and measuring the load-point deflection ($\Delta$) directly from the crosshead displacement of the Instron machine, the Young's modulus was calculated. There was some variation in the Young's modulus, as computed using Equation 5, at various load-point displacements. An average value of Young's modulus was calculated and used in plotting the bending stress-strain data in Figure 21.

Table 5 shows the results for three-point bending on CSA specimens at different temperatures. The bending stress-strain curves at room temperature (21°C) and at cryogenic temperature (-196°C) are shown in Figure 21. The curves are linear with an average flexural modulus of 167 MPa at room temperature and 360 MPa at cryogenic temperature (-196 °C).

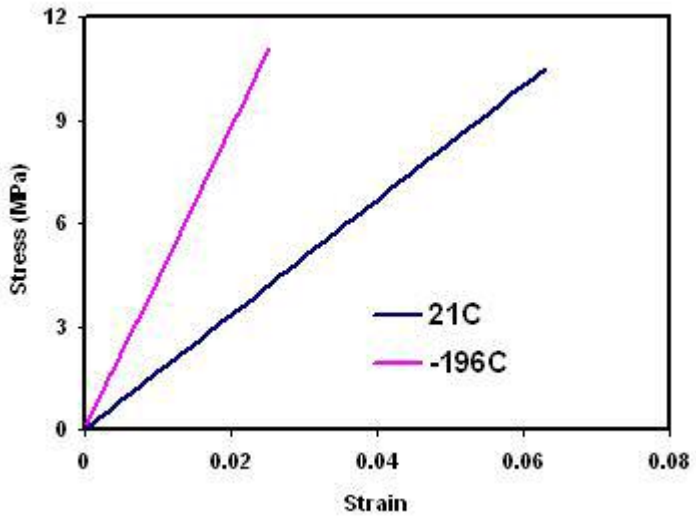


**Figure 21 Three point bend tests on crosslinked silica aerogel**

The flexural modulus at –196 °C is almost double that at room temperature, and the flexural strength (~11 MPa) showed a slight increase, thereby confirming the capability of CSA to sustain bending loads at cryogenic temperatures.

Figure 22 shows the load-deflection curves for crosslinked silica aerogel at 180 °C. As seen from the figure, the curves are nonlinear. There was considerable variation in both, load and deflection data. Equation 5 was not used for calculating the flexural modulus, as it's only applicable for small deformations in linear elastic region. The failure loads and deflections are tabulated in Table 5.

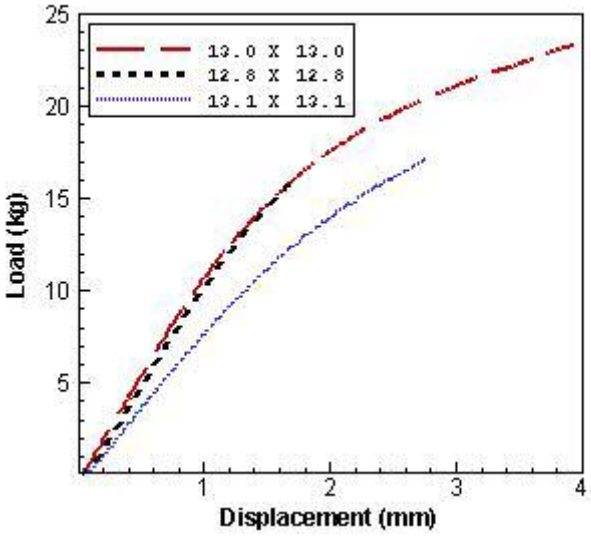


**Figure 22 Load-Deflection curves for crosslinked silica aerogel at 180 °C**

| Temperature | Failure Load (kg) | Square Dimm. (mm) | Failure Disp. (mm) | Young's Modulus (MPa) | Flexural Strength (MPa) |
|---|---|---|---|---|---|
| 1 (21° C) | 21.93 | 13.9 | 1.90 | 181 | 11.99 |
| 2 (21° C) | 19.15 | 13.9 | 1.77 | 160 | 10.48 |
| 3 (21° C) | 15.18 | 13.7 | 1.58 | 160 | 8.67 |
| Average (21° C) | 18.75 | | | 167 | 10.38 |
| 4 (-196° C) | 20.6 | 13.5 | 0.855 | 360 | 11.50 |
| 5 (-196° C) | 17.8 | 13.8 | 0.558 | 517 | 10.6 |
| Average (-196° C) | 19.2 | | | 438.5 | 11.05 |
| 6 (-180° C) | 15.93 | 13.0 | 1.68 | --- | --- |
| 7 (-180° C) | 23.29 | 12.8 | 2.77 | --- | --- |
| 8 (-180° C) | 17.16 | 13.1 | 3.94 | --- | --- |
| Average (-180° C) | 18.79 | | | --- | --- |

**Table 5 Results for three-point bending on crosslinked silica aerogel**

### 6.3 Numerical modeling of compression experiments in PFC$^{3D}$

Figure 23 shows the cluster structure generated using the DLCA algorithm. The algorithm generates particles according to a Gaussian distribution function, with parameters used to generate the cluster summarized in Table 6. The DLCA code output gives the radius of the each particle and its location in 3D space, which is subsequently supplied to the PFC3D input file. The bounds of the cell size were chosen so as to have a cell size as large as possible, without compromising computational efficiency, and minimizing code run time. A total of 2400 particles were generated, with a aerogel porosity of 71.92 %.

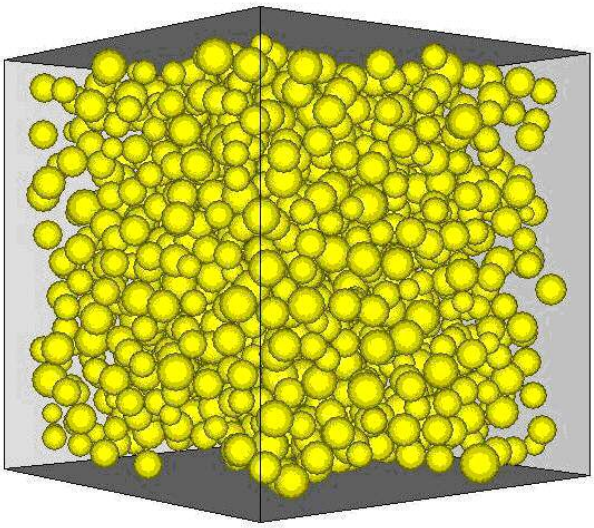

**Figure 23 Cluster structure generated using DLCA algorithm**

| Parameter | Value |
|---|---|
| Cell size, L | 1000 Å |
| Number of particles, N | 1200 |
| Mean particle size, $r_0$ | 75 Å |
| Standard deviation, σ | 25 Å |
| Diffusion parameter, α | -0.55 |
| Step size, Δ | 30 Å |

**Table 6 Parameters used in the DLCA algorithm**

Once the model is setup it is calibrated using the procedure described in Section 5.3, the values of the normal and shear particle stiffness are estimated using equation 1. The expected Young's modulus of the particle-particle contact (micro-modulus) is equated to the actual modulus (macro-modulus) estimated from the compression experiment i.e. 128Mpa. The value for R is chosen as the average radius of particles, i.e. 35nm. Using

these values the initial normal and shear stiffness is estimated to be 18N/m. The parallel bond stiffness, $k_{np}$, was calculated using equation 3. The Young's modulus of the parallel bond was taken same as the experimental compressive modulus, which was then divided by the length of bond between the two particles in contact. Using $E_p$=128 MPa and the length of the bond to be 70nm the estimated $k_{np}$ is $1.83\times10^{15}$ N/m. The shear bond stiffness $k_{sp}$ is taken to be same as the normal bond stiffness. The values for normal and shear bond strengths is equal to the failure strength of the assembly i.e. 190MPa

Figure 24 shows the calibration curve for the normal particle stiffness. The compressive modulus varies with the normal particle stiffness from which a relationship, which is approximately linear, is observed as predicted by equation 1. Also the particle stiffness is related to the strength of the model. Figure 25 shows the calibration curve for compressive strength at 77% with the normal particle stiffness. The micro-mechanical parameter values determined from calibration curves and used in the uniaxial loading simulations, and are summarized in table 7. Though the structural and other parameters such as bond strength and stiffness remained unchanged the calibration curve does not show a perfectly linear elastic behavior as expected from the equation (1). The reason, for this discrepancy, is that the level of equilibrium achieved from $PFC^{3D}$ simulations show a change as the particle stiffness was varied, thereby affecting Young's modulus.

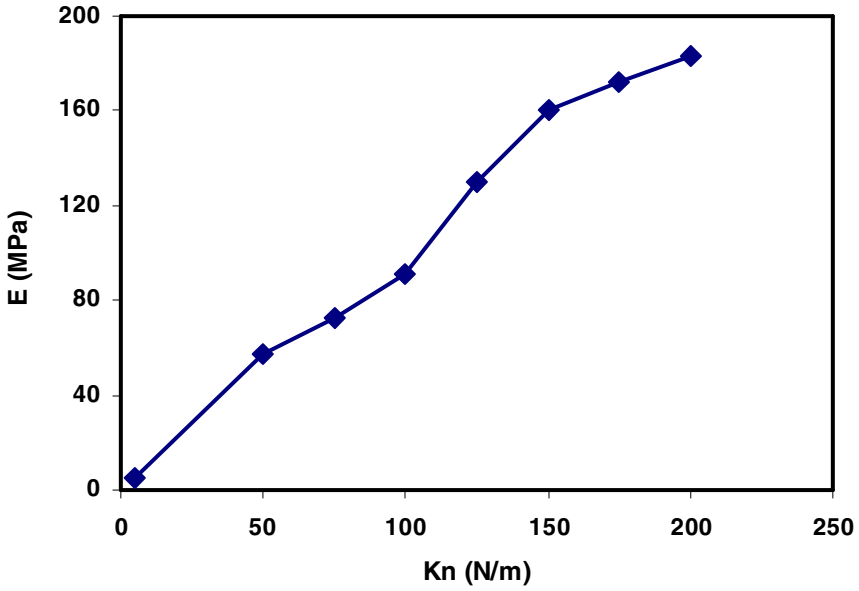


**Figure 24 Calibration curve showing the variation of compressive modulus of particle assembly with the normal stiffness of particle**

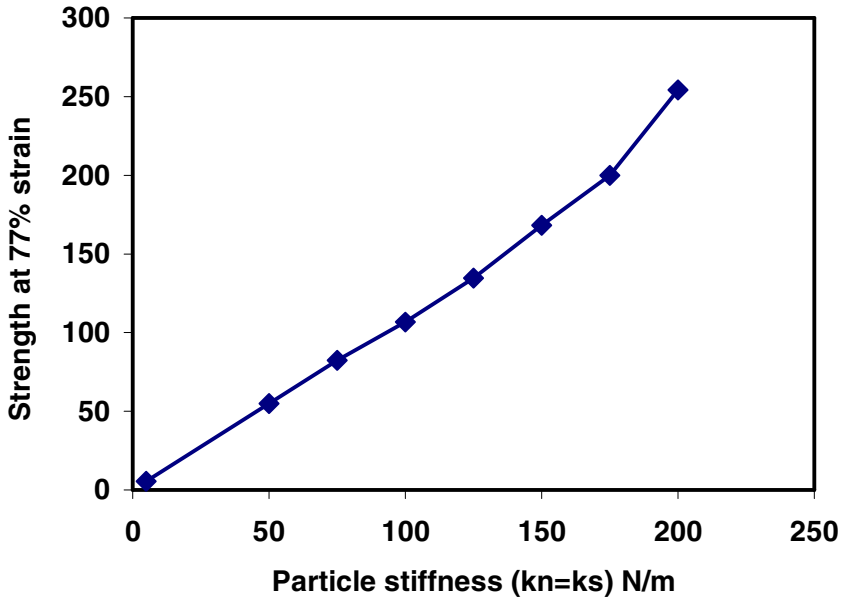


**Figure 25 Calibration curve showing the variation of compressive strength at 77% strain of particle assembly with the normal stiffness of particle**

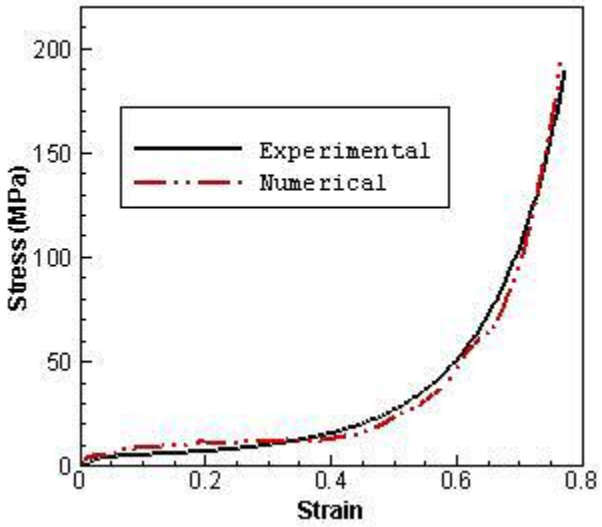


**Figure 26 Stress-strain curves from experiment and simulation of compression**

| | Value | Units |
|---|---|---|
| **BALL PARAMETERS** | | |
| Density | 480 | $kg/m^3$ |
| Normal stiffness | 135 | N/m |
| Shear stiffness | 130 | N/m |
| Friction | 0.6 | |
| **BOND PARAMETERS** | | |
| Radii | $3.50X10^{-8}$ | .m |
| Normal stiffness | $1.82\ X10^{15}$ | N/m |
| Shear stiffness | $1.82\ X10^{15}$ | N/m |
| Normal strength | $190\ X10^{6}$ | MPa |
| Shear strength | $190\ X10^{6}$ | MPa |
| **WALL PARAMETERS** | | |
| Normal stiffness | $1\ X10^{10}$ | N/m |
| Shear stiffness | $1\ X10^{10}$ | N/m |
| Wall disp | $0.2\ X10^{-10}$ | .m |
| **POROSITY** | 79.82 | % |
| **STRUCTURE PARAMETERS** | | |
| Type of distribution | | Gaussian |
| mean dia of ball | $7.5\ X10^{-9}$ | .m |
| Deviation | $2.50\ X10^{-9}$ | .m |
| Cell size | $(1X1X2)\ X10^{-7}$ | .m |

**Table 7 Parameters used in PFC3D simulation**

PFC3D can be used in a fully predictive mode where enough data of high quality are available or it can be used as a numerical laboratory to test design ideas in a data limited system. Most of the development on aerogel modeling in this study is based on limited available data. The most important factor is the structure of the numerical specimen as PFC3D models are categorized as direct, damage-type numerical models in which the deformation is not a function of prescribed relationships between stresses and strains, but of changing microstructure. Small changes in structure can bring about large changes in the failure mechanism of the model. In this study the DLCA algorithm was used to generate the loop structure, which is very important to account for the stiffness of the aerogel. It can be seen from Figure 23 that there is an abundance of dead-ends in the aerogel network. Dead ends are clusters connected to the backbone of the aerogel at only one point. Figure 27 is a snapshot of the uniaxial compression simulation at 40% strain.

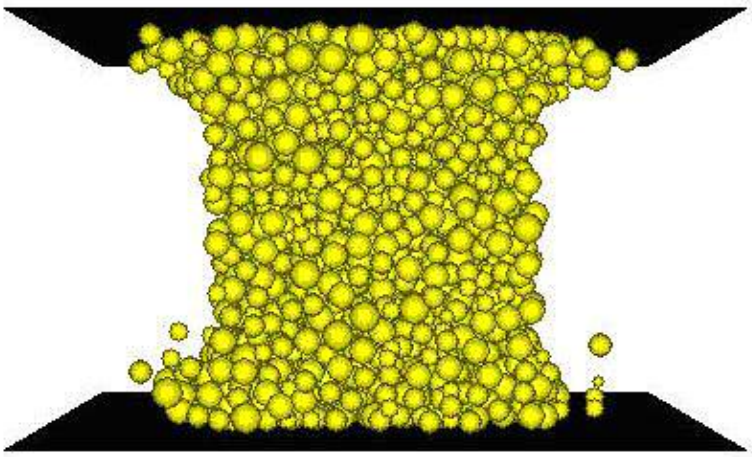

**Figure 27 Uniaxial compression simulation of aerogel at 40 % strain**

As seen from the figure the failure of the model is not similar to what is expected from the experiments, with few particles separating from the core assembly. These particles are the ones contributing to the dead ends. As the load increases, the bond between the particles with the cluster structure held by a single contact breaks which makes these particles to break from the core assembly. The dead-ends do not contribute to the stiffness of the model, which can be seen from the nature of the stress strain curve. Moreover, the model is not in a desired state of equilibrium because of the very high porosity (70-80%). At such high porosity, there are very few contacts with neighboring particles, which tends to allow particles to be in a state of continuous motions. . Figure 28 is a snapshot of the uniaxial compression simulation at 77% strain

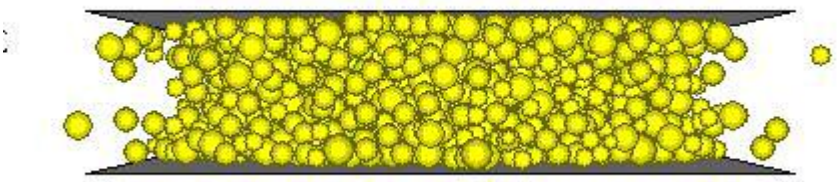

**Figure 28 Uniaxial compression simulation of aerogel at 77 % strain**

**Sensitivity Study**

Sensitivity analysis was performed on the numerical model by varying one parameter at a time. The key parameters affecting the behavior of the model were identified, by performing trial runs. The effects of the identified key parameters on the behavior of simulation curves are described in the following paragraphs. The particle stiffness is the most important parameter affecting the nature of the curve. Figure 29 shows the effect of

increase in ball stiffness (both normal and shear stiffness assumed equal) on the stress-strain behavior of the model.

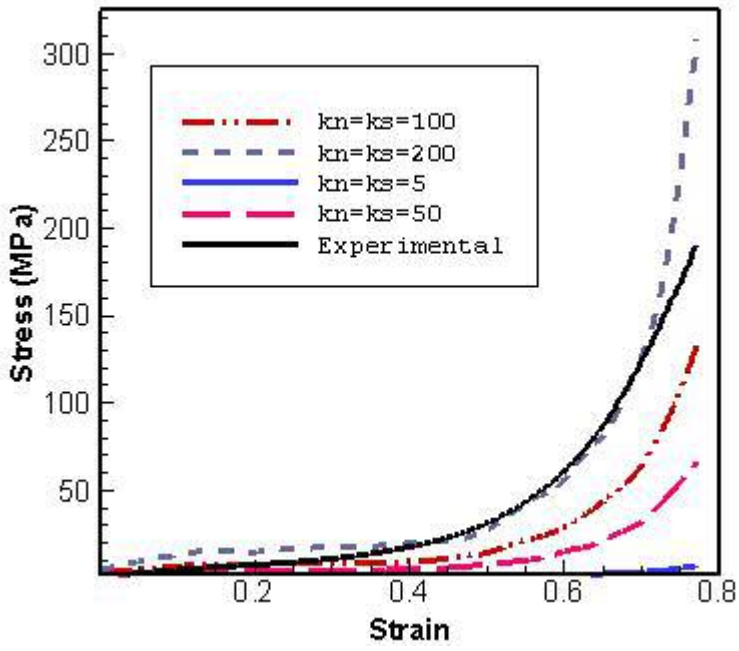


**Figure 29 Effect of change in stiffness of particles on behavior of simulation model**

As the stiffness of the particle is increased, both the Young's modulus and the strength of the model, at 77% strain, increases with a relationship, which is approximately linear as shown in Figures 22 & 23.

The particle stiffnesses were then altered in different ratios to study the effects between them. Figure 30 shows the effect of particle normal stiffness ($k_n$) held constant at 140 N/m while the particle shear stiffness ($k_p$) being varied. As seen there is little effect of on the strength at 77% strain. Whereas, there is a significant change in the behavior of stress strain curves when the particle shear stiffness ($k_p$) was hel constant at 140 N/m and the particle normal stiffness ($k_n$) varied. As this ratio of shear to normal particle stiffness increases the curve shifts upwards as seen in Figure 31

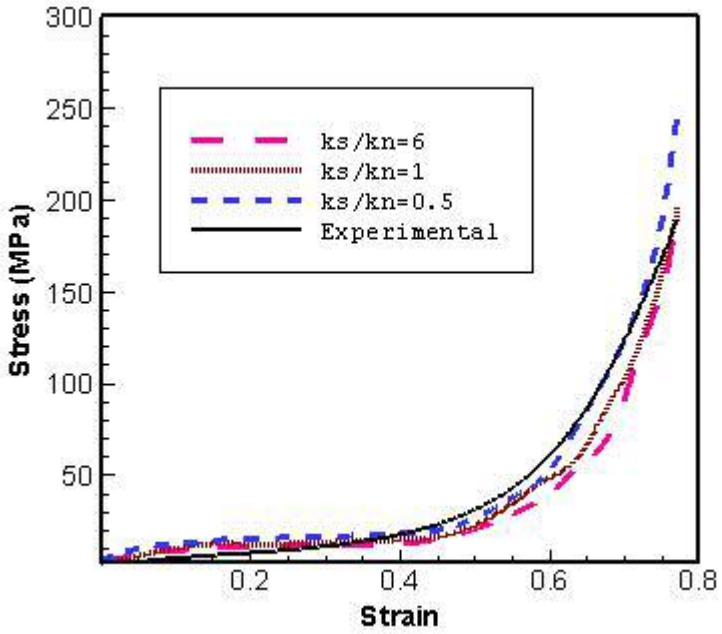


**Figure 30 Effect of change in normal stiffness of particles ($k_s$=140 N/m =constant) on behavior of simulation model**

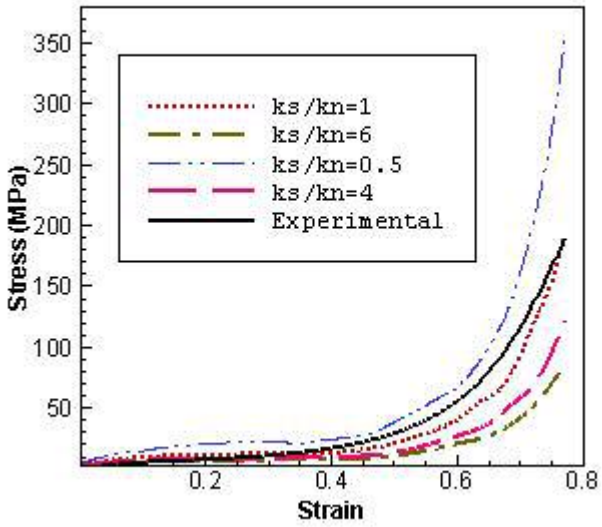


**Figure 31 Effect of change in shear stiffness of particles ($k_n$=140 N/m =constant) on behavior of simulation model**

The effect of particle coefficient of friction (μ) on the nature of stress strain curve was studied by varying μ in the range 0.01 to 1.0. With increase in particle coefficient of

friction the curve shift upwards i.e. the slope of the stress-strain curve in the granular region increases as shown in Figure 32. This is attributed to the predominance of slip model once the bonds in the model have broken. As the coefficient of friction increase more force is required to compress the balls and hence the increase in slope in the granular region.

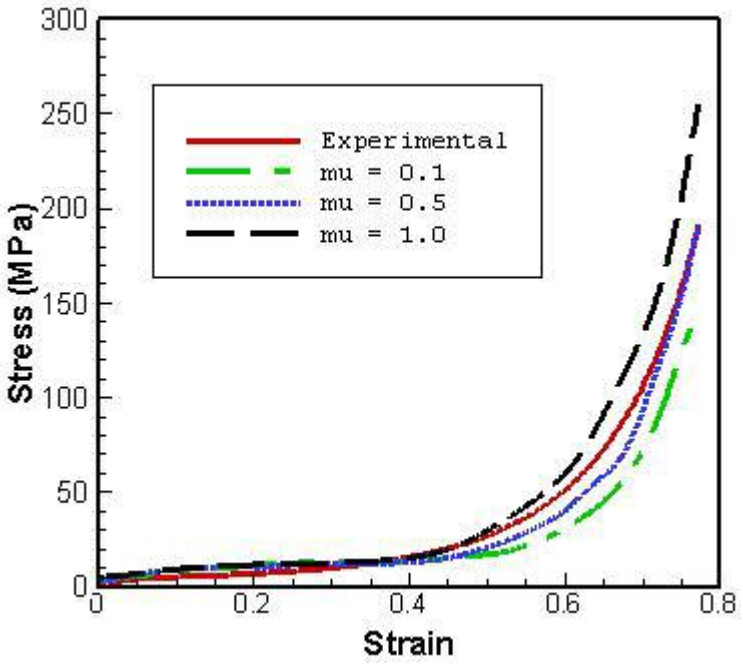


**Figure 32 Effect of change in particle friction coefficient on behavior of simulation model**

Surprisingly there is a little effect of increase in particle density on the nature of the curve as shown in Figure 33. With increase in particle density the strength at 77% strain increases marginally.

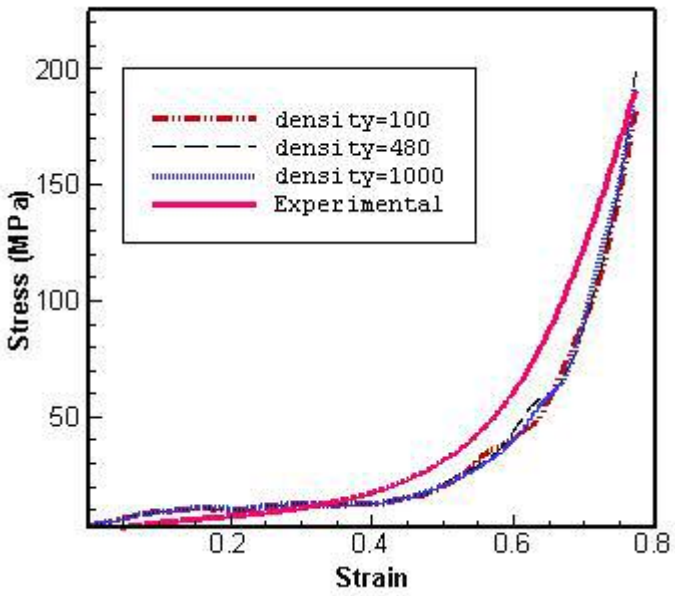


**Figure 33 Effect of change in particle density (kg/m$^{3)}$ on behavior of simulation model.**

# CHAPTER 7

# CONCLUSIONS AND FUTURE WORK

Basic mechanical characterization experiments of uniaxial compression and flexure were conducted on crosslinked silica aerogel. The findings are as follows.

- The compressive strength of crosslinked silica aerogel is greatly improved from 5 MPa to 128 MPa as compared with plain silica aerogels, without much sacrifice in the density. The specific compressive strength is higher than the conventional material and comparable to that of aerospace grade graphite-epoxy composite laminates.
- Aerogels exhibits a scaling relationship of relative strength against relative density. The scaling exponent was determined to be 4.14, higher compared to the value reported in literature in the range 3 to 3.5.
- A numerical model ($PFC^{3D}$) was developed as a first step towards modeling of silica aerogels. The aerogel network structure was found to be an important factor affecting the failure mechanism. Good agreement between the experimental and numerical stress-strain curve were observed.

**Future work**

- An algorithm needs to be developed, that will eliminate the dead-end particles or transform the dead-end particles to form loops.
- Failure mechanisms in $PFC^{3D}$ are sensitive to the model structure. Even if the dead-ends modifying algorithm is developed, the data for porosity of model will increase the reliability of the input parameters, which at present are assumed. The porosity of crosslinked silica aerogel can be measured by a technique such as nitrogen adsorption/desorption.
- Modeling of three point bending and tensile specimens needs to be addressed. This will increase the confidence of the quantitative parameters obtained from compression simulation. Parallel processing option should be employed to model the three point bending simulations which will have large size.

# REFERENCES


1. Wu, M., Liao, C., "Polymorphism in nylon 6/clay nanocomposites", Macromolecular Chemistry and Physics**,** Volume 201, Issue 18, Pages 2820 - 2825
2. Garcés, J., Moll, J., Bicerano, J., Fibiger, R., McLeod, D., "Polymeric Nanocomposites for Automotive Applications" Advanced Materials,Volume 12, Issue 23, 2000. Pages 1835-1839
3. Cassignol, C.,Olivier, P., Ricard, A., "Influence of the dopant on the polypyrrole moisture content: Effects on conductivity and thermal stability", Journal of Applied Polymer Science, Volume 70 (1998), Issue 8 , Pages 1567- 1577
4. "Experimental study of aerogel Cherenkov detectors for particle identification Nuclear Instruments and Methods in Physics Research Section A" Accelerators, Spectrometers, Detectors and Associated Equipment, Volume 374, Issue 3, 1 June 1996, Pages 286-292
5. Domínguez, G., Westphal, A., Jones, S., and Phillips, M., "Energy loss and impact cratering in aerogels-theory and experiment" Icarus, Volume 172, Issue 2, December 2004, Pages 613-624
6. Hrubesh, L., "Technical Applications of Aerogels", 5th International Symposium on Aerogels Montpellier, France September 8-10, 1997
7. http://www.ep2.physik.uni-wuerzburg.de

8. Woignier, T., Phalippou, J., "Mechanical strength of silica aerogels," Journal of Non-Crystalline Solids 100 (1988) 404-408
9. Parmenter, K., Milstein, F., "Mechanical properties of silica aerogel," Journal of Non-Crystalline Solids 223 (1998) 179-189
10. Takahashi, R., Sato, S., Sodesawa, T., Goto, T., Matsutani, K., Mikami, N., "Bending strength of silica gel with bimodal pores: Effect of variation in mesopore structure" Materials Research Bulletin, Volume 40, Issue 7, 12 July 2005, Pages 1148-1156
11. Moner-Girona, M., Martinez, E., Roig, A., Esteve, J., Molins, E., "Mechanical properties of silica aerogels measured by microindentation: influence of sol-gel processing parameters and carbon addition" Journal of Non-Crystalline Solids 285 (2001) 244-250
12. Martin, J., Hosticka, B., Lattimer, C., Norris, P., " Mechanical and acoustical properties as a function of PEG concentration in macropourous silica aerogels" Journal of Non-Crystalline Solids 285 (2001) 222-229
13. Despetis, F., Etienne, P., Etienne-Calas, S., "Subcritical crack growth in silica aerogel" Journal of Non-Crystalline Solids, Volume 344, Issues 1-2, 15 September 2004, Pages 22-25
14. Perin, L., T., Faivre, A., Calas-Etienne, S., Woignier, T., "Nanostructural damage associated with isostatic compression of silica aerogels" Journal of Non-Crystalline Solids, Volume 333, Issue 1, 1 January 2004, Pages 68-73

15. Scherer, G., Smith, D., Qiu, X., Anderson, J., "Compression of aerogels" Journal of Non-Crystalline Solids 186 (1995) 2 June 1995, Pages 316-320

16. Miner, M., Hosticka, B., Norris, P., "The effects of ambient humidity on the mechanical properties and surface chemistry of hygroscopic silica aerogel" Journal of Non-Crystalline Solids, Volume 350, 15 December 2004, Pages 285-289

17. Gross, J., Reichenauer, G., Fricke, J., "Mechanical properties of silica aerogels" Journal of Physics. D: Applied Physics. **21** 1447-1451

18. H. Ma, A. Roberts, J. Prevost, R. Jullien, and G. Scherer, "Mechanical Structure-Property Relationship of Aerogels," J. of Non-Crystalline Solids, 277 (2000) 127-141.

19. L.J. Gibson, M.F. Ashby, Cellular Solids: Structure and Properties, Pergamon, New York, 1988.

20. Gavalda, S., Kaneko, K., Thomson, K., Gubbins, K., "Molecular modeling of carbon aerogels" Colloids and Surfaces A: Physicochemical and Engineering Aspects, Volumes 187-188, 31 August 2001, Pages 531-538

21. Nicholas Leventis, C. Sotiriou-Leventis, G. Zhang, and A. Rawashdeh, "Nanoengineering Strong Silica Aerogels," Nano Letters, 2002, Vol. 2, No. 9, 957-960.

22. Zhang, G., Dass, A., Rawashdeh, A., Thomas, J., Joseph A., Sotiriou-Leventis, C., Fabrizio, E., "Isocyanate-crosslinked silica aerogel monoliths: preparation and characterization" Journal of Non-Crystalline Solids, Volume 350, 15 December 2004, Pages 152-164

23. Bouaziz, J., Bout-ret, D., Sivade, A., Grill, C., "Journal of Non-Crystalline Solids", (1992), 145,71.

24. Ruben, G.C., Hrubesh, L.W. and Tillotson, T.M., "High resolution transmission electron microscopy nanostructure of condensed-silica aerogels" Journal of Non-Crystalline Solids, Volume 186, 2 June 1995, Pages 209-218

25. Hasmy, A., Vacher, R. and Jullien, R., "Small-angle scattering by fractal aggregates: A numerical investigation of the crossover between the fractal regime and the Porod regime**",** Physical Review B, 1994,50,1305.

26. Hasmy, A., Anglaret, E., Foret, M., Pelous, J. and Jullien, R., "Small-angle neutron-scattering investigation of long-range correlations in silica aerogels: Simulations and experiments", Physical Review B, 1994,50,6006.

27. Yokogawa, H. and Yokoyama, M., "Hydrophobic silica aerogels**"** Journal of Non-Crystalline Solids, Volume 186, 2 June 1995, Pages 23-29

28. Wang, J., Shen, J., Zhou, B., Deng, Z., Zhao, L., Zhu, L., Li, Y., "Cluster structure of silica aerogel investigated by laser ablation" Nanostructured Materials, Volume 10, Issue 6, August 1998, Pages 909-916

29. R. Botet, R. Jullien, M. Kolb, J. Phys. A 17 (1984) L75.

30. Meakin, P., Family, F., "Structure and dynamics of reaction-limited aggregation", Phys. Rev. A 36, 5498–5501 (1987)

31. T. M. Haard, Ph.D thesis, Northwestern University, 2001 (unpublished).

32. Itasca, Particle flow code in 3 dimensions, version 3.0, User's manual. Itasca Consulting Group, Inc 2003

33. ASM Engineering Materials Handbook, Composites, Volume 1, May 1988, Table 2 Pg 178.

34. Kulatilake, P., Malama, B., and Wang,.J, "Physical and particle flow modeling of jointed rock block behavior under uniaxial loading" International Journal of Rock Mechanics and Mining Sciences, Volume 38, Issue 5, July 2001, Pages 641-657

# APPENDIX A

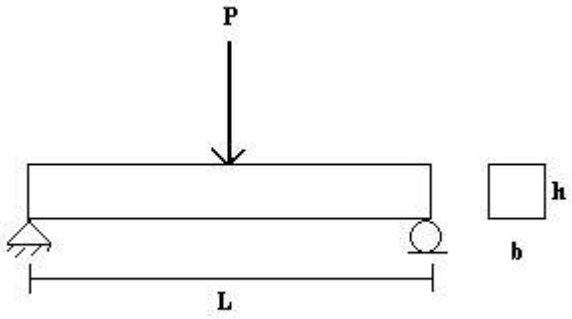


The samples tested in three-point bending had small spans and therefore the effect of shear needs to be accounted in the point-load deflection

The

$$U = \frac{P^2 L^3}{96EI} + \frac{3P^2 L}{5AG}$$

Applying Castigliano's theorem to get the load-point defection

$$\delta = \frac{\partial U}{\partial P} = \frac{PL^3}{48EI} + \frac{6PL}{5AG}$$

Substituting $G = \frac{E}{2(1+\nu)}$ in above equation we get

$$\delta = \frac{PL^3}{48EI} + \frac{12PL(1+\nu)}{5AE}$$

$$\delta = \frac{PL^3}{48EI}\left[1 + \frac{576I(1+\nu)}{5AL^2}\right]$$

Substituting $I = \frac{bh^3}{12}$ for a rectangular cross-section of width 'b' and height 'h' and rearranging the terms we get

$$\delta = \frac{PL^3}{48EI}\left[1 + \frac{48(1+\nu)}{5}\left(\frac{h}{L}\right)^2\right]$$

From above equation 'E' can be determined by

$$E = \frac{PL^3}{48\delta I}\left[1 + \frac{48(1+\nu)}{5}\left(\frac{h}{L}\right)^2\right]$$

# VITA

Nilesh Shimpi

Candidate for the Degree of

Master of Science

Thesis: MECHANICAL TESTING AND NUMERICAL SIMULATION OF MECHANICAL STRUCTURE-PROPERTY RELATIONSHIP OF SILICA AEROGEL

Major Field: Mechanical Engineering

Biographical:

Personal data: Born in Mumbai, India, On December 21, 1979, the son of Nathu and Sarojini Shimpi.

Education: Received Bachelor of Engineering degree in Mechanical Engineering from University of Mumbai, India in June 2001. Completed requirements for Master of Science degree with a major in Mechanical and Aerospace Engineering at Oklahoma State University in December 2005.

Experience: Graduate Research Assistant in Mechanical and Aerospace Engineering Department, Oklahoma State University, Stillwater, Oklahoma, August, 2003 – present. Graduate Teaching Assistant in Mechanical and Aerospace Engineering Department, Oklahoma State University, Stillwater, Oklahoma, January, 2003 –May, 2004.

Name: Nilesh Shimpi Date of Degree: December, 2005

Institution: Oklahoma State University Location: Stillwater, Oklahoma

Title of Study: MECHANICAL TESTING AND NUMERICAL SIMULATION OF MECHANICAL STRUCTURE-PROPERTY RELATIONSHIP OF SILICA AEROGEL

Pages in Study: 66 Candidate for the Degree of Master of Science

Major Field: Mechanical Engineering

**Scope and Methodology of Study:** Silica aerogel are highly porous nanostructured solids materials with wide range of applications. However silica aerogels are inherently fragile and brittle. Thus, their use in load-bearing applications presents a challenge. Mechanical behavior of nanostructured silica aerogel is characterized under compression and three-point bending tests. In order to develop a better understanding of the synergistic stiffening and strengthening mechanism of the crosslinker a numerical model was developed using Particle Flow Code.

**Findings and Conclusions:** The compressive strength increased 40 times the strength of plain silica aerogels. Testing was also carried out under different strain rates and temperatures. In flexural tests the stress-strain curve obtained showed a perfect elastic behavior and the "conchoidal" fracture morphology. The results from numerical modeling emphasis need for a better algorithm that can generate the silica aerogel structure. Also the quantitative parameters determined from modeling need to be experimentally validated.

ADVISER'S APPROVAL: Dr. Samit Roy